



Mass-loss Rates for O and Early B Stars Powering Bow Shock Nebulae: Evidence for Bistability Behavior

Henry A. Kobulnicky¹ , William T. Chick¹, and Matthew S. Povich²

¹ Department of Physics & Astronomy, University of Wyoming, Dept. 3905, Laramie, WY 82070-1000, USA; chipk@uwyo.edu

² Department of Physics & Astronomy, California State Polytechnic University, 3801 West Temple Avenue, Pomona, CA 91768, USA

Received 2018 September 13; revised 2019 June 1; accepted 2019 June 3; published 2019 July 19

Abstract

Second only to initial mass, the rate of wind-driven mass loss determines the final mass of a massive star and the nature of its remnant. Motivated by the need to reconcile observational values and theory, we use a recently vetted technique to analyze the mass-loss rates in a sample of OB stars that generate bow shock nebulae. We measure peculiar velocities from new *Gaia* parallax and proper motion data and their spectral types from new optical and infrared spectroscopy. For our sample of 70 central stars in morphologically selected bow shock nebulae, 67 are OB stars. The median peculiar velocity is 11 km s^{−1}, significantly smaller than classical “runaway star” velocities. Mass-loss rates for these O and early B stars agree with recently lowered theoretical predictions, ranging from $\approx 10^{-7} M_{\odot} \text{ yr}^{-1}$ for mid-O dwarfs to $10^{-9} M_{\odot} \text{ yr}^{-1}$ for late O dwarfs—a factor of about 2.7 lower than the often-used Vink et al. formulation. Our results provide the first observational mass-loss rates for B0–B3 dwarfs and giants— 10^{-9} to $10^{-8} M_{\odot} \text{ yr}^{-1}$. We find evidence for an increase in the mass-loss rates below a critical effective temperature, consistent with predictions of the bistability phenomenon in the range $T_{\text{eff}} = 19,000\text{--}27,000$ K. The sample exhibits a correlation between modified wind momentum and luminosity, consistent in slope but lower by 0.43 dex in magnitude compared to canonical wind–luminosity relations. We identify a small subset of objects deviating most significantly from theoretical expectations as probable radiation-driven bow wave nebulae by virtue of their low stellar-to-nebular luminosity ratios. For these, the inferred mass-loss rates must be regarded as upper limits.

Key words: H II regions – stars: massive – surveys

1. Introduction

The rate at which massive stars expel material in radiation-driven winds is a fundamental factor in their evolution. Large mass-loss rates reduce final core masses and, thereby, determine the type of supernova that ensues, as well as the nature of the final compact object (e.g., white dwarf, neutron star, black hole, or none). For the $\approx 50\%$ of massive stars that have close companions (Kobulnicky & Fryer 2007; Sana et al. 2012; Kobulnicky et al. 2016), mass exchange and common envelope evolution may become the overriding evolutionary influences. But for single massive stars, stars with distant companions (effectively single), and even in close binaries prior to interaction, wind mass loss removes copious amounts of envelope material on timescales relevant to the rapid evolution of such stars. Measured mass-loss rates, \dot{M} , lie in the range $< 10^{-9}$ to a few $\times 10^{-6} M_{\odot} \text{ yr}^{-1}$, depending on the stellar mass and evolutionary stage (e.g., Garmany et al. 1981; Howarth & Prinja 1989; Fullerton et al. 2006; Mokiem et al. 2007; Marcolino et al. 2009; Prinja & Massa 2010). Kudritzki & Puls (2000), Puls et al. (2008), and Smith (2014) provide comprehensive reviews of massive star winds and mass loss.

Measurements of mass-loss rates at any given spectral type and luminosity class span orders of magnitude. H α , radio continuum, and infrared observations measure the excess above the stellar photosphere and constitute the class of “ n^2 ” diagnostics, because the extraphotospheric flux scales as the square of the density of material in the wind for optically thin geometries. This class of techniques typically yields mass-loss rates at the upper end of the range and larger than those predicted by theory unless corrected for the effects of “clumping”—density inhomogeneities in the wind (e.g., see Leitherer 1988;

Owocki et al. 1988; Fullerton et al. 1996; Puls et al. 1996, 2005; Martins et al. 2005b; Massa et al. 2017, for discussions of rates and clumping). The other canonical approach, ultraviolet absorption spectroscopy of high-ionization wind lines, typically yields mass-loss rates at the low end of the range and far below many theoretical models (Garmany et al. 1981; Howarth & Prinja 1989; Fullerton et al. 2006; Marcolino et al. 2009). The former techniques become insensitive below rates of about $10^{-7} M_{\odot} \text{ yr}^{-1}$ (Markova et al. 2004; Mokiem et al. 2007; Marcolino et al. 2009), while the latter becomes insensitive above $10^{-7} M_{\odot} \text{ yr}^{-1}$ as many UV resonance lines become saturated. In the limit of weak winds ($\dot{M} \lesssim 10^{-8} M_{\odot} \text{ yr}^{-1}$, $\log(L/L_{\odot}) \lesssim 5.2$), UV-based mass-loss rates fall two orders of magnitude below theoretical expectations. This “weak-wind problem” (Martins et al. 2005b; Mokiem et al. 2007; Marcolino et al. 2009; Muijres et al. 2012), coupled with the limitations of the canonical mass-loss techniques, especially for a whole range of stars later than about O7V, calls for new approaches to diagnosing stellar mass loss. Promising techniques include X-ray (Cohen et al. 2014) or infrared (Najarro et al. 2011) spectroscopy of stellar winds.

A related unsolved problem in stellar winds is the impact of the “bistability” jump, characterized by a sudden increase in Lyman continuum and metal line opacity over a narrow temperature range predicted variously to lie somewhere between 19,000 and 27,000 K³ (Pauldrach & Puls 1990; Lamers et al. 1995; Vink et al. 2000; Petrov et al. 2016), with

³ This is often termed the “first bistability jump,” given the prediction of a “second bistability jump” near 9000–12,000 K owing to a sudden recombination of Fe III to Fe II (Vink et al. 1999; Petrov et al. 2016). In this work, we consider only the former.

modern estimates falling at the low end of this range. This elevated opacity should produce a dramatic increase in mass-loss rate by factors of 3 to as much as 20 and a corresponding decrease in the terminal wind velocity. Observational verification of this putative bistable behavior is very limited. Markova & Puls (2008) observed a small sample of B supergiants on either side of the proposed bistability region and concluded that \dot{M} increases only by factors of a few, if at all. Circumstantial evidence for larger enhancements in \dot{M} comes from the slow rotation rates observed among B supergiants on the cool side of the bistability jump, interpreted as evidence for rotational braking through mass loss (bistability braking; Vink et al. 2010). Our study provides new data on mass-loss rates that will have implications for the effects of bistable behavior in stellar winds.

In Kobulnicky et al. (2018), we refined an underexploited mass-loss measurement strategy, building upon a principle outlined in Kobulnicky et al. (2010) and first proposed by Gull & Sofia (1979). The approach entails the physical principle of momentum flux balance between a highly supersonic stellar wind and the impinging interstellar medium (ISM) around a high-velocity “runaway” (Blaauw 1961; Gies & Bolton 1986) star. Along the surface where the momentum fluxes equate, an arc-shaped shock (bow shock) forms (Wilkin 1996, 2000) that may be detectable in the infrared continuum or emission lines (e.g., O III, H α). While only about 15% of runaway stars have detectable infrared bow shock nebulae (Peri et al. 2015), over 700 candidate bow shocks around probable early-type stars are known (Kobulnicky et al. 2016). Kobulnicky et al. (2018) estimated interstellar densities preceding bow shocks and suggested that ambient number densities exceeding 5 cm^{-3} may be required to produce a detectable infrared bow shock nebula. This may explain why the Galactic latitude scale height of bow shock candidates (0.6° ; Kobulnicky et al. 2016, Figure 3) matches that of the molecular gas in the Milky Way. Identified most commonly by their $24 \mu\text{m}$ morphologies, the majority of arcuate nebulae also have corresponding $70 \mu\text{m}$ nebulae (Kobulnicky et al. 2017).

The mass-loss rates for such stars may be expressed in terms of quantities that are, in principle, observable:

$$\dot{M} = \frac{4\pi R_0^2 V_a^2 \rho_a}{V_w}. \quad (1)$$

R_0 is the “standoff distance” between the star and the bow shock nebula, computed from an angular size on infrared images and a known distance. V_w is the terminal stellar-wind speed, typically adopted from the literature according to the spectral type and luminosity class. V_a is the velocity of the star relative to the local ISM, which may be computed from distance, proper motion, and radial velocity data in conjunction with a Galactic rotation curve model. Finally, ρ_a is the density of the ambient ISM, which Kobulnicky et al. (2018) estimated from the $70 \mu\text{m}$ infrared surface brightness using Draine & Li (2007, DL07) dust emission coefficients and assuming a preshock/postshock density ratio of 1:4, appropriate for strong shocks. In convenient astrophysical units, the mass-loss rate may be expressed as

$$\dot{M} (M_\odot \text{ yr}^{-1}) = 1.67 \times 10^{-28} \times \frac{[R_0(\text{arcsec})]^2 D(\text{kpc}) [V_a(\text{km s}^{-1})]^2 I_\nu(\text{Jy sr}^{-1})}{V_w(\text{km s}^{-1}) \ell(\text{arcsec}) j_\nu(\text{Jy cm}^2 \text{ sr}^{-1} \text{ nucleon}^{-1})}. \quad (2)$$

Here, j_ν is the frequency-dependent dust emission coefficient per nucleon as a function of ambient radiant energy density parameter from the star’s illuminating flux at the distance of the infrared nebula, U .⁴ U , in turn, may be obtained by knowing the standoff distance, the stellar luminosity from its effective temperature and radius, because the central star dominates the local radiation field by factors of 100 or more (Kobulnicky et al. 2017).

Finally, I_ν is the observed infrared surface brightness at the corresponding frequency. We use the surface brightnesses and scaled DL07 dust emission coefficients at $70 \mu\text{m}$ owing to the availability of *Herschel Space Observatory* (HSO) measurements in that band, but other wavelengths may eventually be proven suitable. We avoid using the $24 \mu\text{m}$ *Spitzer Space Telescope* (SST) or $22 \mu\text{m}$ *Wide-Field Infrared Survey Experiment* (WISE) bandpasses because of the likelihood that this wavelength regime may be dominated by a population of stochastically heated very small grains (Draine & Li 2007). The path length through the nebula is given by the observed angular chord diameter, ℓ . D is the distance to the star and nebula.

Our approach has the distinction of being rooted in a fundamentally different principle from other mass-loss measurement techniques. As such, we expect it to be insensitive to some of the uncertainties that limit other methods. Because the bow shocks typically lie several tenths of a parsec from the star, small-scale effects of wind clumping or temporal fluctuations in wind speed or density should be minimized through spatial and temporal averaging. At the same time, our technique is subject to its own set of assumptions and approximations.

1. We assume isotropic stellar winds. But mass loss could be enhanced along the polar axis or reduced at the equatorial plane for rapidly rotating stars (Owocki et al. 1996; Langer 1998; Müller & Vink 2014).
2. We assume a homogeneous ISM. This is appropriate, on average, but certain to be incorrect for many real astrophysical examples.
3. Our approach assumes that the velocity of the impinging ISM is directed radially in the frame of the star. Bulk flows of interstellar material at oblique angles relative to a moving star have been considered theoretically (Wilkin 2000) and should produce asymmetric bow shock nebulae with morphologies similar to some of those cataloged in Kobulnicky et al. (2016). Such complications are beyond the scope of this effort.
4. The 1:4 pre-/postshock density ratio we adopt to estimate the interstellar density preceding the shock is merely a physically motivated assumption appropriate for strong nonradiative shocks. Density ratios in regions that experience significant cooling in radiative shocks could be more extreme. Hydrodynamical simulations of OB star bow shocks show that density ratios may reach factors of 10 over small scales that are well below the observational resolution limits. Factors of 4 are about right when averaged over the $\simeq 0.1\text{--}0.3 \text{ pc}$ scales typical of sample objects (e.g., Figures 7 and 4, respectively, of Comeron & Kaper 1998; Meyer et al. 2017).

⁴ $U = \frac{u_*}{u_{\text{MMP83}}} = \frac{R_*^2 \sigma T_{\text{eff}}^4 / (R_0^2 c)}{u_{\text{MMP83}}}$, where $u_{\text{MMP83}} = 0.0217 \text{ erg s}^{-1} \text{ cm}^{-2} / c$, given by Mathis et al. (1983).

5. It should be remembered that the measured geometrical quantities such as R_0 are projected quantities only. We apply a statistical correction factor of $1/\sin(65^\circ) = 1.10$ for inclination effects when computing R_0 in parsec. This is a suitable correction because inclinations substantially smaller than about 50° would begin to mask the arcuate morphology and make the object unlikely to be included in the list of bow shock candidates (e.g., see Acreman et al. 2016 for numerical simulations of bow shocks at various inclination angles). Given the large variation in signal-to-noise ratios (S/Ns) of infrared images, we have not attempted to derive inclination angles for each object using geometrical properties of the nebulae (e.g., Tarango-Yong & Henney 2018).
6. We assume that the DL07 dust emission coefficients are appropriate to bow shock nebulae, where a combination of radiative and shock heating may exist. In Section 2.2, we describe a rescaling of these coefficients made necessary by the harder radiation field of early-type stars compared to the interstellar radiation field. These dust models are constructed for dust that is radiatively heated. Kobulnicky et al. (2017) found that the dust color temperatures of bow shock nebulae were systematically above those expected from steady-state radiative heating from the central stars, leading them to propose this difference as evidence for shock heating, although this signature could also result from stochastically heated grains (A. Li 2019, private communication). Additional heating by shocks could elevate dust emission coefficients beyond those adopted here. If shock heating is present but not properly accounted for, the adopted dust emission coefficients could be too small, and the resulting mass-loss rates too large (see Equation (2)). On the contrary, Henney & Arthur (2019) argues that stellar-wind particles do not propagate across the termination shock into the swept-up dusty region of the nebulae, and so shock heating is negligible.

Kobulnicky et al. (2018) employed the principle of momentum balance for 20 bow-shock-generating OB stars with known distances. They found stellar mass-loss rates factors of 10 or more lower than canonical n^2 diagnostics for a homogeneous wind, factors of 10 greater than UV absorption-line determinations, and factors of ≈ 2 lower than recent theoretical mass-loss predictions (Vink et al. 2001; Lucy 2010). They concluded that, once corrected for geometrical clumping and porosity in velocity space, theoretical models would produce \dot{M} predictions consistent with the bow shock method measurements. They further noted that the technique showed promise for measuring mass-loss rates for weak-winded late O and early B stars, but there were not enough B stars in their sample to draw meaningful conclusions. Furthermore, uncertainties on the Kobulnicky et al. (2018) mass-loss rates were large and dominated by uncertainties on the stellar velocities (assumed there to be 30 km s^{-1} for lack of direct measurement) and uncertainties on the distances to the stars.⁵ Because \dot{M} in Equation (2) scales as the square of both V_a and D in this technique (D , via the distance dependence implicit within the derived U parameter on which dust emission coefficients are based), their results were highly sensitive to errors on these quantities.

With the availability of the *Gaia* mission Data Release 2 (GDR2) data products (Gaia Collaboration et al. 2018), excellent parallaxes and proper motions—therefore, distances and peculiar velocities—are now available for an enlarged sample of bow-shock-generating stars. In Kobulnicky et al. (2016), we compiled an “all-sky”⁶ catalog of 709 bow shock candidates consisting of arcuate infrared nebulae enclosing symmetrically placed stars. In Kobulnicky et al. (2017), we presented mid-IR photometry for the catalog of 709 bow shock candidates using archival *SST*, *WISE*, and *HSO* images. In this contribution, we extend the proof-of-concept sample of Kobulnicky et al. (2018) to measure mass-loss rates for stars having well-measured distances, velocities, and infrared bow shock properties. This expanded sample includes a greater fraction of early B stars and represents the first attempt at mass-loss determinations for dwarfs in this stellar temperature and luminosity regime. Section 2 describes the selection of sample targets and computation of requisite parameters. Section 3 details the selection of the sample of stars for analysis. Section 4 presents the mass-loss rates with a comparison to previous literature results and theoretical model predictions. Section 5 summarizes the implications for mass-loss prescriptions and for the evolution of massive stars.

2. New Data

2.1. Infrared and Optical Spectra from the Apache Point Observatory

We acquired new optical spectra of 15 candidate bow shock stars using the Double Imaging Spectrograph (DIS)⁷ at the Apache Point Observatory (APO) 3.5 m telescope on the nights of 2018 May 12 and 19, and June 13. The 1200 line mm^{-1} gratings in both the red and blue arms of the spectrograph yielded reciprocal dispersions of 0.58 and $0.62 \text{ \AA pix}^{-1}$, respectively, over wavelength ranges $5700\text{--}6900 \text{ \AA}$ and $4200\text{--}5500 \text{ \AA}$, respectively. Exposure times ranged from $2 \times 300 \text{ s}$ to several $\times 600 \text{ s}$ depending on source magnitude, yielding spectra with S/Ns between 30:1 and 100:1 at 5900 \AA . Seeing ranged between $1''.6$ and $4''.0$ in a $1''.5 \times 110''$ slit aligned at the parallactic angle, owing to the large airmass for the southern targets. The instrument HeNeAr lamps supplied periodic wavelength calibration to an rms of 0.006 \AA in the red channel and 0.1 \AA in the blue channel. Instrument rotation produces wavelength shifts of up to 0.3 pix during the night, which were removed by periodic arc lamp exposures so that the wavelength solutions are estimated to be precise to about 5 km s^{-1} based on repeated observations of the same star. On nights with good seeing where the FWHM of the point-spread function was comparable to the slit width, placement of the star within the slit may contribute additional velocity uncertainties. Observations of one or more radial velocity standard stars (HD 196850, HD 185270, and HD 182758) indicate that the velocity calibration is accurate to about 10 km s^{-1} in the worst cases. We assign a minimum radial velocity uncertainty of 6 km s^{-1} to each star. Data reductions employed internal quartz lamp flat-fielding and local sky subtraction adjacent to the star. Continuum normalization produced one-dimensional spectra suitable for spectral classification and radial velocity

⁵ The DL07 dust emission coefficients tabulated in Kobulnicky et al. (2018) are also affected by an interpolation error for objects with $U < 10^4$.

⁶ The visual search for arcuate $24 \mu\text{m}$ nebulae was confined to regions near the Galactic Plane where both early-type stars and mid-infrared surveys from the *SST* are concentrated.

⁷ <https://www.apo.nmsu.edu/arc35m/Instruments/DIS/>

measurement after velocity correction to the heliocentric reference frame using the IRAF⁸ `rvcor` task.

We observed 25 stars (four of these were also observed with the DIS optical spectrograph) using the TripleSpec (Wilson et al. 2004) infrared cross-dispersed echelle spectrograph at APO on the nights of 2017 July 13, 2017 August 30, 2017 September 1 and 8, 2017 October 9, 2018 May 29, and 2018 June 3 and 24. The spectrograph yields continuous spectral coverage between 0.95 and 2.4 μm at a resolution of about $R \simeq 3500$ (85 km s^{-1}) using a $1''.1$ slit aligned at the parallactic angle. Four or eight 60–120 s exposures were obtained over an airmass range of 1.0–4.7 using a standard ABBA nod pattern on targets ranging from $H = 7$ to $H = 12$ mag, yielding spectra with S/Ns between 20:1 and 80:1 in the H band near 1.6 μm . Seeing averaged $1''.2$ – $1''.8$. Reductions involved flat-fielding using internal quartz lamps and wavelength calibration using night-sky emission lines adjacent to the target star, yielding (vacuum) wavelengths to a precision of about 0.7 Å ($\simeq 10 \text{ km s}^{-1}$). Observations of three radial velocity standard stars HD 182758 ($V_{\odot} = +2 \text{ km s}^{-1}$), HD 185270 ($V_{\odot} = -23 \text{ km s}^{-1}$), and HD 196850 ($V_{\odot} = -21 \text{ km s}^{-1}$) indicate that the radial velocities are accurate to within about $\pm 12 \text{ km s}^{-1}$. This low instrumental precision is a consequence of the fact that the infrared point-spread function was sometimes smaller than the $1''.1$ slit width, causing the star to wander in the dispersion direction within the slit. We assign a minimum radial velocity uncertainty of 6 km s^{-1} to each star. Several A0V stars were observed over the range of target airmasses to aid in the removal of the telluric absorption features. Reductions were performed using the APOTripleSpec tool IDL package, a modified version of the SpeX tool package (Cushing et al. 2004). Spectra were then transformed to the heliocentric velocity frame using the IRAF `rvcor` task and continuum normalized, treating the JHK -band portions of the spectrum separately.

We have supplemented these new spectroscopic data with 19 stars observed in the red portion of the optical spectrum with the optical longslit spectrograph at the Wyoming Infrared Observatory (WIRO; to be reported in W. T. Chick et al. 2019, in preparation). Table 1 lists the source of spectroscopy for each target using a single-character code for optical data from the APO (O—24 instances), infrared data from the APO (I—16 instances), optical data from W. T. Chick et al. (2019, in preparation), (C—19 instances), and spectral types adopted from the literature (L—23 instances). Twelve objects have observations from more than one observatory or wavelength regime. In all, we have our own spectra for 47 of the 70 stars. The Appendix provides a summary of spectral classifications for each object.

The optical and/or infrared spectra were used to classify the stars and measure radial velocities. Most stars were only observed on a single night. Eight stars have both optical and infrared spectra, allowing for a comparison of radial velocities between the two regimes. The overwhelming majority of the stars show He I features—notably 5875.65 Å or 2.1126 μm —indicative of O and early B stars hotter than about 15,000 K. A few show He II at 5410 Å or 2.1885 μm , a signature of stars earlier than about 09. The equivalent widths of the He lines and

(if available) the ratios of He II/He I allow us to designate a spectral type for most stars to within about one subtype by reference to stellar atmospheric models (Tlusty; Lanz & Hubeny 2003) or the infrared spectral atlas of hot stars (Hanson et al. 1996). Stellar atmospheric features in our observed wavelength range are relatively insensitive to temperature for stars in the B1–B4 range, and observed spectral lines (mostly He I and H I) are greatly degenerate between temperature and gravity. Hence, spectral classifications are more uncertain in this regime. The available spectral diagnostics are not especially sensitive to gravity, so, in most cases the luminosity class is not well constrained from the spectra alone. However, the addition of parallax distances allows us to distinguish between dwarf, giant, and supergiant luminosity classes: at a given distance, only one luminosity class is consistent with the 2MASS JHK photometric data, once interstellar reddening is removed. We measure and remove interstellar extinction using the Rayleigh–Jeans H – $4.5 \mu\text{m}$ color excess method of Majewski et al. (2011). The Appendix contains a brief discussion of the spectral classification, distance, and radial velocity (with notes on possible binarity) for each star in the sample.

2.2. Rescaled Dust Emission Coefficients

Kobulnicky et al. (2018) used the dust emission coefficients of DL07, which are appropriate for an incident radiation spectrum similar to the mean interstellar one (Mathis et al. 1983), peaking in the red or near-IR portion of the spectrum. However, the spectrum from OB stars illuminating bow shock nebulae is much harder, peaking in the ultraviolet. Henney & Arthur (2019) concluded, on the basis of modeling an assortment of grain compositions using Cloudy (Ferland et al. 2017), that it was necessary to scale the DL07 emission coefficients upward by about a factor of 3 across a range of $10^2 < U < 10^5$ in order to replicate the emission coefficients at the same value of U . Henney & Arthur (2019, Figure 4) state that this is equivalent to using a DL07 model with a factor of about 8 larger U . In the absence of tabulated data, we performed Cloudy modeling to compare the emissivity of standard ISM dust grains at 70 μm illuminated by a hot, $T = 28,000 \text{ K}$, $\log g = 4.0$ star (Castelli & Kurucz 2003) typical of our sample to emissivities illuminated by an interstellar radiation field (table `ism` in Cloudy) with the same radiation density. We define this ratio of emissivities $f_j \equiv j(T = 28000)/j(\text{ISRF})$. Figure 1 plots f_j versus the radiation density parameter over the range of our sample objects, $U = 10^2$ – 10^5 . The black curve shows a polynomial fit to this relationship, $f_j(U) = 0.14[\log U]^2 - 1.42[\log U] + 5.16$. At the low end of the range, this ratio exceeds 3, while at high radiation densities, it asymptotically approaches 1.5. Varying the modeled stellar effective temperature from 18,000 to 45,000 K, representing the full range in our sample, shows that this ratio varies by about 15% across this wide range in temperature. Hence, a case-by-case, source-specific modeling effort would be appropriate as part of a future effort. In this present analysis, we will adopt the $f_j(U)$ from Figure 1 as a scale factor to increase the emission coefficients relative to nominal DL07 values to better approximate those expected in the UV-intense environments of bow shock nebulae. The net effect will be to decrease the derived mass-loss rates by factors of 1.5–3, with a median of 2.0. The correction is more significant for objects with lower radiation densities. These

⁸ Tody (1986); IRAF is distributed by the National Optical Astronomy Observatories, which are operated by the Association of Universities for Research in Astronomy, Inc., under cooperative agreement with the National Science Foundation.

Table 1
Measured and Adopted Parameters for Stars and Their Bow Shock Nebulae

ID	Name	Alt. Name	Sp.T.	T_{eff}	R_*	Mass	V_∞	D	R_0	R_0	Peak ₇₀	ℓ	Obs.	L_*/L_{IR}
(1)	(2)	(3)	(4)	(K)	(R_\odot)	(M_\odot)	(km s^{-1})	(pc)	(arcsec)	(pc)	(10^7 Jy sr^{-1})	(arcsec)	(14)	(15)
1	...	G000.1169−00.5703	O8V	35500	9.4	26.0	2000.0	2441	26.4	0.344	166	39	0.3	252
3	...	G001.0563−00.1499	B5III:	15000	8.0	7.0	500.0	1527	6.2	0.05	432	12	0.4	11
7	...	G003.8417−01.0440	B2V	20600	5.4	10.9	700.0	1313	8.6	0.06	764	27	0.4	61
11	...	G005.5941+00.7335	B0V	29000	7.4	17.5	1200.0	2446	7.6	0.099	15	13	0.3	1389
13	Zeta Oph	G006.2812+23.5877	O9.2IV	31000	7.2	19.0	1300.0	112	299.0	0.179	12	277	0.3	1735
16	...	G006.8933+00.0743	B0III	29000	15.0	20.0	1200.0	3008	29.0	0.465	83	23	0.3	807
26	...	G011.0709−00.5437	O9V	31500	7.7	18.0	1200.0	3060	8.2	0.134	24	7	0.4	532
28	...	G011.6548+00.4943	B0V	29000	7.4	17.5	1200.0	2409	9.2	0.118	33	26	0.3	330
32	...	G012.3407−00.3949	B2V+B2V	20600	5.4	10.9	800.0	2398	7.5	0.096	64	13	0.4	73
46	...	G014.4703−00.6427	B2V:	20600	5.4	10.9	700.0	688	14.7	0.054	33	28	0.4	45
67	NGC 6611ESL45	G017.0826+00.9744	O9V	31500	7.7	18.0	1300.0	1507	7.5	0.06	256	7	0.3	44
83	...	G019.8107+00.0965	B8II	11000	15.0	20.0	700.0	2709	5.6	0.081	49	11	0.5	460
100	...	G023.0958+00.4411	B1V	26000	6.4	14.2	800.0	1819	6.7	0.065	39	12	0.3	144
101	...	G023.1100+00.5458	B0V	29000	7.4	17.5	1200.0	2330	12.7	0.158	199	34	0.3	48
129	TYC 5121-625-1	G027.3338+00.1784	M0III	3800	40.0	1.2	...0	870	11.2	0.052	232	11	0.0	4
163	...	G031.9308+00.2676	B3II	17000	11.0	14.0	600.0	4438	15.5	0.367	33	18	0.5	31
201	...	G037.2933+00.6703	B2V	20600	5.4	10.9	800.0	1088	7.6	0.044	36	13	0.0	162
289	...	G055.5792+00.6749	M0III	3800	40.0	1.2	...0	2138	34.0	0.388	38	33	0.0	0
320	HD 191611	G073.6200+01.8522	O9III	30700	13.6	23.0	1300.0	2509	35.5	0.475	53	21	0.4	1056
322	...	G074.3117+01.0041	O8IV:	32500	14.1	27.0	2000.0	4460	19.5	0.464	46	20	0.3	1998
331	LSII+39 53	G078.2869+00.7780	O7V	35500	9.3	26.0	2500.0	1594	42.0	0.357	48	55	0.3	296
333	...	G078.5197+01.0652	B0V+B0V	30900	7.4	17.5	2500.0	1554	28.9	0.24	66	16	0.4	461
338	CPR 2002A10	G079.8223+00.0959	O8V:	33400	8.5	22.0	2000.0	1792	23.0	0.22	319	29	0.3	138
339	CPR 2002A37	G080.2400+00.1354	O5V	41500	11.1	37.0	2900.0	1703	70.0	0.636	103	47	0.3	640
341	KGK 2010-1	G080.8621+00.9749	O9V	31500	7.7	18.0	1300.0	1622	20.0	0.173	19	31	0.4	379
342	KGK 2010-2	G080.9020+00.9828	B4V	15500	4.3	6.5	800.0	1538	10.0	0.082	231	14	0.4	22
344	BD+43 3654	G082.4100+02.3254	O4If	40700	19.0	58.0	3000.0	1577	193.0	1.623	234	170	0.3	247
353	...	G104.3447+02.2299	O5V	41500	11.1	37.0	2900.0	3932	30.5	0.64	19	20	0.4	8563
356	HD 240015	G106.6327+00.3917	B0III	29000	15.0	20.0	1000.0	2583	15.6	0.215	13	15	0.4	22422
357	HD 240016	G106.6375+00.3783	B2III	20900	15.0	20.0	700.0	1493	21.8	0.174	13	25	0.3	16066
361	TYC 4278-522-1	G108.9891+01.5606	B1Ia	20000	25.0	25.0	800.0	3896	91.7	1.905	13	75	0.5	1974
362	...	G109.1157+00.6799	B2I	17600	40.0	23.0	700.0	5295	14.7	0.415	16	27	0.4	1999
367	LSI+60 226	G133.1567+00.0432	O7V	35500	9.4	26.0	2500.0	2131	36.0	0.409	28	51	0.3	4812
368	KM Cass	G134.3552+00.8182	O8.5V	32500	8.5	22.0	2000.0	2298	14.0	0.172	99	22	0.3	3804
369	BD+60 586	G137.4203+01.2792	O8III	32500	14.0	27.0	2000.0	2762	73.0	1.075	31	39	0.3	646
380	HD 53367	G223.7092−01.9008	B2Ve:	20600	5.4	17.5	700.0	130	22.0	0.015	143	49	0.3	2479
381	HD 54662	G224.1685−00.7784	O7Vz	35500	9.4	26.0	2500.0	1142	220.0	1.34	18	200	0.4	688
382	FN Cma	G224.7096−01.7938	B0III	28000	15.0	20.0	1200.0	934	101.0	0.503	44	70	0.8	1547
384	CD-35 4415	G253.7104−00.1920	O7IIInn	34600	14.5	31.0	2500.0	3791	31.0	0.627	93	23	0.3	1204
391	HD 77207	G268.9550−01.9022	B7Iab +	11000	50.0	20.0	500.0	1851	32.0	0.316	16	27	0.5	1863
392	CPD-47 3051	G269.2089−00.9138	B0V	29000	7.4	17.5	1200.0	1901	28.0	0.284	21	39	0.3	691
394	HD 298310	G272.5794−01.7247	B0V	29000	15.0	20.0	1200.0	2199	21.0	0.246	26	45	0.4	867
395	HD 298353	G273.1192−01.9620	O7V	35500	9.4	26.0	2500.0	2685	32.0	0.458	33	23	0.3	1794
397	CD-55 3196	G282.1647−00.0256	O9.5III	30200	13.4	21.0	1200.0	2513	22.0	0.295	99	28	0.3	288
404 ^a	CD-59 3123	G286.0498−01.6583	O9.5Ib	28400	23.0	30.0	1200.0	3969	54.0	1.143	31	70	0.4	449
405	HD 303197	G286.4644−00.3478	B3III	17000	11.0	14.0	600.0	2328	21.0	0.261	49	27	0.4	44

Table 1
(Continued)

ID	Name	Alt. Name	Sp.T.	T_{eff} (K)	R_* (R_{\odot})	Mass (M_{\odot})	V_{∞} (km s^{-1})	D (pc)	R_0 (arcsec)	R_0 (pc)	Peak ₇₀ (10^7 Jy sr^{-1})	ℓ (arcsec)	Obs.	L_*/L_{IR}
(1)	(2)	(3)	(4)	(5)	(6)	(7)	(8)	(9)	(10)	(11)	(12)	(13)	(14)	(15)
406	HD 92607	G287.1148−01.0236	O9IVn	31100	10.0	20.0	1300.0	2786	15.8	0.235	116	26	0.3	195
407	HD 93249	G287.4071−00.3593	O9III+O	30700	13.6	23.0	1300.0	3096	7.8	0.129	232	25	0.3	88
409	HD 93027	G287.6131−01.1302	O9.5IV	30300	7.4	16.0	1200.0	3426	7.4	0.135	83	17	0.3	147
410	HD 305536	G287.6736−01.0093	O9.5V+ B	30500	7.4	16.0	1200.0	2266	3.7	0.045	366	14	0.3	227
411	HD 305599	G288.1505−00.5059	O9.5V	30500	7.4	16.0	1200.0	2071	4.2	0.046	166	6	0.3	757
413	HD 93683	G288.3138−01.3085	O9V+B0V	31500	7.7	18.0	1300.0	1629	15.0	0.13	61	28	0.3	709
414	HD 93858	G288.4263−01.2245	B3II	17000	11.0	14.0	600.0	2602	5.8	0.08	26	13	0.4	1481
463	TYC 8995-1548-1	G308.0406+00.2473	B0III:	28000	15.0	20.0	1200.0	3689	15.9	0.313	26	19	0.4	2459
555	ALS 18049	G326.7256+00.7742	O9V:	31500	7.7	18.0	1300.0	2677	4.1	0.059	465	14	0.3	16
589	CD-49 10393	G332.4863+00.8256	B0V	29000	7.4	17.5	1200.0	2533	9.5	0.128	51	37	0.4	219
624	...	G340.4772−00.1528	B0III	29000	15.0	20.0	1200.0	3508	18.4	0.344	49	38	0.3	515
626	...	G340.8579−00.8793	O9V	31500	7.7	18.0	1300.0	2169	11.5	0.133	698	24	0.3	20
634	HD 152756	G342.3422−00.4456	B0III	28000	15.0	20.0	1200.0	1802	32.0	0.308	33	43	0.4	309
635	...	G342.5873+00.1600	O6V	38100	10.2	32.0	2800.0	3197	31.0	0.529	96	45	0.5	83
637	...	G342.7172−00.4361	B2V	20600	5.4	10.9	700.0	1315	5.8	0.041	8	7	0.3	210
648	...	G344.4658−00.5580	B0III	29000	15.0	20.0	1200.0	1893	14.8	0.149	68	44	0.3	530
653	...	G346.1388−00.2184	K0III:	4000	15.0	1.1	...	1664	1.9	0.017	31	14	0.0	1
655	...	G346.2958+00.0744	B1V:	26000	6.4	14.2	800.0	2168	3.5	0.04	66	13	0.3	366
673	...	G349.5431−00.5952	B1V:	26000	6.4	14.2	800.0	2705	6.0	0.087	23	15	0.3	1200
692	...	G353.4162+00.4482	O7V	35500	9.3	26.0	2500.0	1717	34.0	0.311	515	55	0.4	102
694	...	G355.4972−00.7571	B2V:	20900	5.4	10.9	700.0	1329	5.8	0.041	21	14	0.3	704
700	...	G356.6602+00.9209	B0V	29000	7.4	17.5	1200.0	3370	15.8	0.284	13	21	0.3	1202
709	...	G359.9536−00.5088	B0V+B1V	29000	7.4	17.5	1200.0	3091	11.2	0.185	16	11	0.4	49

Note. (1) Identifier from Kobulnicky et al. (2016), (2) common name, (3) generic identifier in Galactic coordinates, (4) spectral classification, primarily from this work and citations herein, (5) adopted effective temperature based on spectral classification using the theoretical scale of Martins et al. (2005a) and extrapolated to early B stars as in Pecaut & Mamajek (2013), (6) stellar radius based on spectral classification using the theoretical scale of Martins et al. (2005a), (7) adopted stellar mass, (8) adopted terminal wind velocity from Mokiem et al. (2007), (9) adopted distance, from *Gaia* parallax-based distances estimated by Bailer-Jones et al. (2018), (10) standoff distance in arcsec, (11) standoff distance in pc using the adopted distance and angular size adjusted by a statistical factor of 1.1 for projection effects, (12) peak 70 μm surface brightness above adjacent background, (13) angular diameter of the nebula in arcseconds defined by a chord intersecting the location of the peak surface brightness, (14) source of spectroscopy, described in the text, and (15) ratio of stellar to infrared nebular luminosity.

^a This object was incorrectly identified in Kobulnicky et al. (2016). The star's coordinates and name have been corrected here.

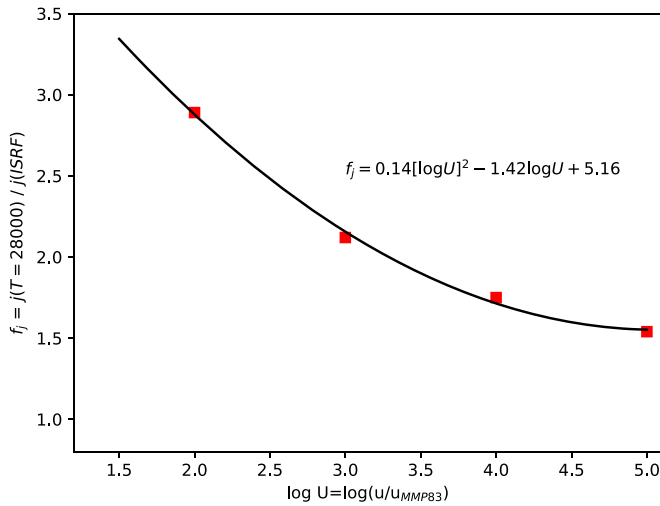


Figure 1. Ratio of *Cloudy*-derived dust emissivities, f_j , illuminated by a hot $T = 28,000$ K source, to emissivities illuminated by an interstellar radiation field having the same radiation density vs. radiation density parameter, U .

larger emission coefficients lead to reduced mass-loss rates compared to those in Kobulnicky et al. (2018), and all values here supersede that work.

We further note that our factor of 1.5–3 corrections to the DL07 dust emission coefficients, as indicated by Figure 1, are about $1.6\times$ smaller than those adopted by Henney & Arthur (2019, Figure 4), which rely solely on *Cloudy* modeling. In other words, a direct comparison of dust emissivities from DL07 and those derived from *Cloudy* models for the same radiation density parameter and the same nominal interstellar radiation field and dust composition show that the former are a factor of about 1.6 smaller than the latter. We are unable to identify a reason for this difference (A. Li 2019, private communication). Hence, the absolute values of the dust emission coefficients should be regarded to entail a systematic uncertainty at the level of 60% until systematic differences between DL07 and the dust implementation in *Cloudy* can be resolved.

2.3. Distinguishing Bow Shocks from Radiation Bow Waves

Henney & Arthur (2019) articulated the physical distinction between stellar-wind-driven bow shocks and a class of “radiation bow waves” and “radiation bow shocks” that may appear morphologically similar but originate from radiation rather than stellar-wind pressure as the dust and gas in a nebula become optically thick. Their Figure 2 distinguishes between these regimes as a function of three parameters: the stellar peculiar velocity, the standoff distance, and ambient interstellar density. It appears that our hottest and highest velocity stars typically fall into the regime of true wind bow shocks, but a few objects, particularly the cooler ones, fall into the “radiation bow wave” regime. In the latter case, our derived mass-loss rates would become upper limits, as both stellar wind and radiation pressure play a role. We make a crude assessment of the physical status of each bow shock using the ratio of stellar luminosity to infrared nebular luminosity, L_*/L_{IR} . This ratio ought to be large (e.g., >50) for true bow shocks when the dust optical depth is low and the nebula reprocesses a very small fraction of the stellar luminosity. Henney & Arthur (2019) analyzed the 20 bow shock stars presented in Kobulnicky et al. (2018) and concluded that all but two were likely to be true

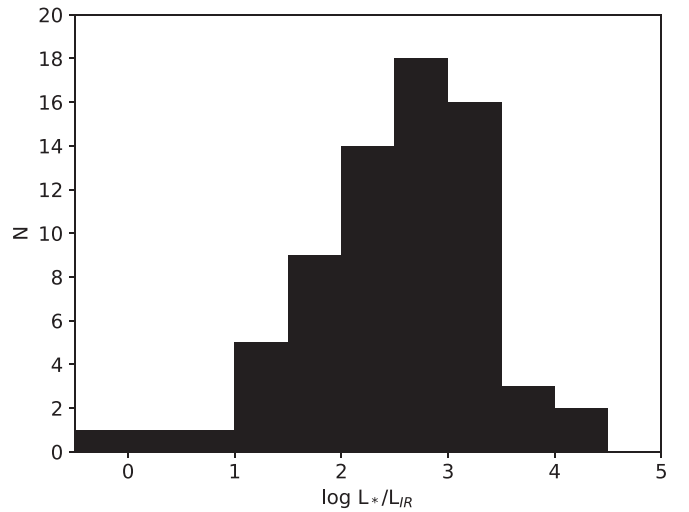


Figure 2. Histogram of the logarithm of the stellar luminosity to infrared nebular luminosity for the 70 objects in this sample. In objects with low values of L_*/L_{IR} , the dust nebulae reprocess a significant fraction of the stellar luminosity, implying an appreciable optical depth for UV photons. The three lowest values are the three late-type stars in our sample.

bow shocks. In particular, object #342 in the numeration of Kobulnicky et al. (2016) with $L_*/L_{\text{IR}} = 22$ is identified as an example of a trapped ionization front driving a radiation bow wave (Henney & Arthur 2019). Figure 2 presents a histogram of L_*/L_{IR} for the sample. The three lowest bins show the three late-type stars in our sample that have $L_*/L_{\text{IR}} < 10$. We will tentatively regard the objects with $L_*/L_{\text{IR}} < 75$ (15 stars) as candidate bow-wave nebulae, based on the analysis that will follow in Section 4.1. The vast majority of the objects have $L_*/L_{\text{IR}} > 75$, making them likely to be genuine bow shock nebulae.

3. Sample Selection for Measuring \dot{M}

Beginning with the Kobulnicky et al. (2016) table of 709 infrared-selected bow shock candidate stars, we searched the GDR2 for corresponding parallax and proper motion measurements. We found that 486 of the 709 stellar targets had a corresponding entry in the GDR2 within $1''.5$ (a few sources had two *Gaia* entries within that error circle, and the brightest was taken as the most probable source). However, we retained only the 231 stars for which the parallax:uncertainty ratio exceeds 3:1, indicative of a reliable distance. Of these 231, only 94 have bow shock nebulae with secure *HST* 70 μm detections required for estimating ambient densities (Kobulnicky et al. 2017). Distances computed straightforwardly from inverse parallaxes are known to be systematically too large owing to the resulting asymmetry from parallax error uncertainties (Bailer-Jones 2015). Although our 3:1 parallax:uncertainty selection criterion minimizes this bias, we adopt the distances from the Bayesian treatment by Bailer-Jones et al. (2018), which results in 0%–20% (mean of 7%) smaller distances compared to inverse parallax values. We also adopt as uncertainties their 68% confidence limits.

Figure 3 shows the locations on the Galactic plane of the 231 bow shock candidate stars with parallaxes known to 33% or better (filled circles). The Sun is at the center. Concentric circles illustrate 2 and 4 kpc distances. Larger unfilled red circles denote the subset of 94 stars having detectable *HST* 70 μm nebulae. Clusterings within Figure 3 reveal the

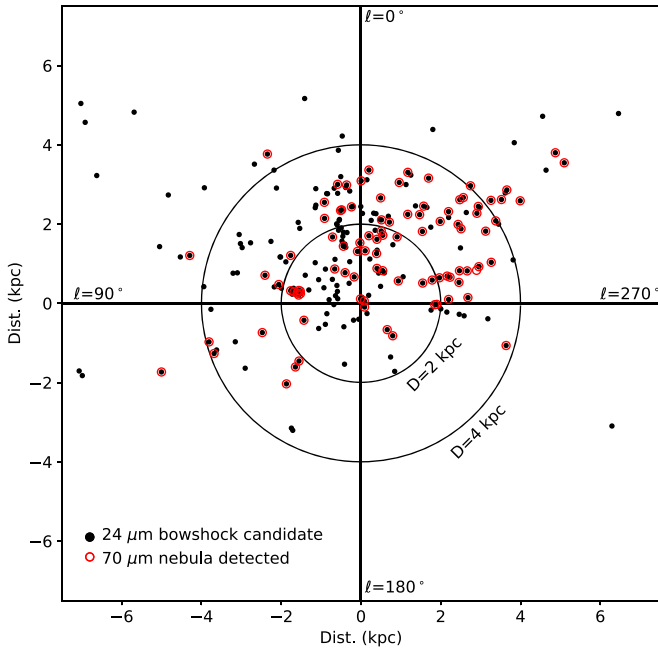


Figure 3. Distribution of 231 bow shock candidate stars having parallax: uncertainty ratios greater than 3:1 on the Galactic plane. The Sun’s location is at the center of the figure. Red circles denote the subset of 94 that have $70\ \mu\text{m}$ photometry from *HST*. In this work, we retain for analysis the 70 of these 94 that have measured spectral types.

concentrations of bow shock OB stars in well-known Galactic associations such as the Cygnus-X region ($\ell \simeq 79^\circ$; $D = 1.4\text{--}1.8\text{ kpc}$) and the Carina complex ($\ell \simeq 287^\circ$; $D = 2\text{--}3.5\text{ kpc}$). The paucity of points in the second and third Galactic quadrants reflects the incomplete *SST* $24\ \mu\text{m}$ survey data in these regions, not necessarily a lower areal density of bow shock candidate objects. The relative lack of sources beyond 4 kpc reflects the reduced sensitivity and angular resolution of *SST* surveys for distant targets in the bright, highly structured, and confused mid-infrared images near the Galactic midplane. Many of the bow shock candidates tabulated in Kobulnicky et al. (2016) are small, near the angular resolution limit of the telescope; more distant sources would appear point-like rather than arc-like and be excluded from the morphologically selected sample. Notably, nearly all of the objects in the fourth quadrant have $70\ \mu\text{m}$ detections, while only about half in the first quadrant do. Finally, Figure 3 does not display obvious signs of a spiral structure that might be traced by the OB stars as representative of young stellar populations. However, the portion of the Galactic plane covered is small, and features more distant than 4 kpc would not be seen using this tracer. As noted by Xu et al. (2018), distance uncertainties on OB stars in GDR2 make discerning spiral structure problematic even for samples much larger than ours. Furthermore, under the (yet-unvalidated and increasingly doubtful) hypothesis that bow shock stars are preferentially runaway stars, they may also fail to trace spiral structure if they have moved significantly from their birth places.

Our intended \dot{M} analysis also requires a measurement of the stellar effective temperature for the calculation of the dust emission coefficient, j_ν . This entails a secure spectral type for each target of interest. Of the 94 star/nebula pairs having parallax and proper motion data and $70\ \mu\text{m}$ detections, we have collected spectral types for 70 stars. Our own optical and

infrared spectra (as described above and in the Appendix) provide the majority of these; a minority come from the literature. A few of the tabulated targets are known or possible binary systems, noted as such in the Appendix. Because multiplicity is high among massive stars (Kobulnicky & Fryer 2007; Sana et al. 2012), there are certain to be other undetected binaries among our sample. Most of the new observations obtained for this work entail only a single epoch of spectroscopy, making binaries difficult to identify. Nevertheless, the near absence of double-lined spectra in our sample suggests that, even in systems containing two or more stars, one star dominates the luminosity. Notably, all but three of the 70 sample stars show He features, confirming that they are, overwhelmingly, OB stars. The remaining three non-OB stars turn out to be two (approximately) M giants (#129 and #289 in the numeration of Kobulnicky et al. 2016) and one K giant (#653). Whether these three late-type stars are responsible for the nearby arcuate nebulae or whether they are unrelated field stars mistakenly identified is unclear. Ultimately, these are inconsequential, in a statistical sense, to the analysis that follows and are not discussed further.

Table 1 lists basic data for the selected subsample of 70 stars. Column 1 contains the index number using the numeration of Kobulnicky et al. (2016). Column 2 lists another common name of the star, followed by the generic name in Galactic coordinates in column 3. Column 4 provides the adopted spectral type/luminosity class, primarily from this work and references cited herein (see the Appendix). Stars with an especially uncertain spectral type are designated by a colon. Columns 5 and 6 contain the adopted effective temperatures and radii, using the theoretical O-star temperature scale and radii from Martins et al. (2005a). For the few B stars, we use the temperatures and radii of Pecaut & Mamajek (2013). Column 7 gives the adopted stellar mass, again from Martins et al. (2005a). Column 8 provides the adopted terminal wind speed calculated by averaging Galactic O and B stars of the same spectral type from Table A.1 of Mokiem et al. (2007) and Table 3 of Marcolino et al. (2009). An alternative approach to estimating terminal wind speeds based on the empirical calibration of Kudritzki & Puls (2000, Equation (9)) yields velocities 1.5 times larger, on average. The net effect of using these values would reduce the derived mass-loss rates by the same factor, on average. Given the different effective temperature scales that undergird that relation, we elect not to adopt these larger terminal wind speeds. The adopted wind speeds are uncertain at the level of 30%, based on the dispersion at a given spectral type, and the fact that we do not have individual terminal wind speed measurements for these stars, which would obviously be desirable. Early B giants and supergiants are particularly uncertain with regard to both their wind speeds and stellar radii. Column 9 lists the parallax-derived distances from Bailer-Jones et al. (2018). The distances used here are generally consistent with those pre-*Gaia* distances used in Kobulnicky et al. (2018), computed from other methods. The largest differences concern the six objects assumed to be part of the Cygnus OB2 Association at the 1.32 kpc eclipsing binary distance (Kiminki et al. 2015) but turn out to be much more distant, 1.7–1.9 kpc, according to *Gaia* parallaxes. Column 10 lists the standoff distance, R_0 , in arcseconds, while column 11 lists the standoff distance in parsec, calculated from the distance in column 9 and the angular separation and the statistical projection factor of 1.1.

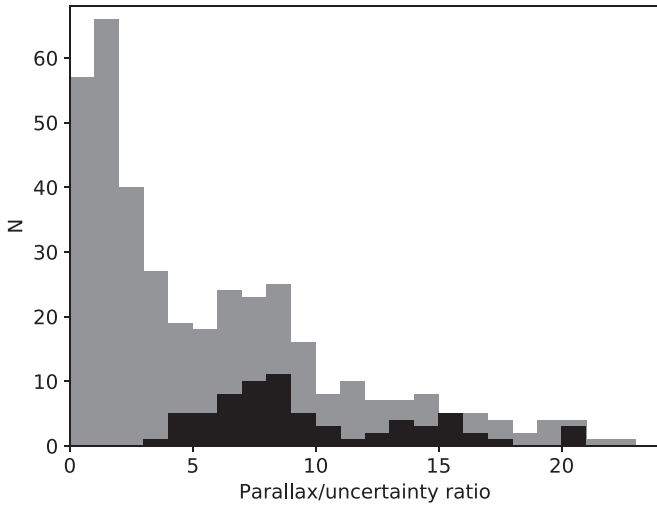


Figure 4. Histogram (gray) of the ratio parallax/uncertainty for the 394 candidate bow shock stars with entries in the GDR2. The black histogram shows the 70 stars retained for further analysis. These have known spectral types, $70\ \mu\text{m}$ detections, and at least a 3:1 parallax:uncertainty ratio.

Column 12 lists the peak $HSO\ 70\ \mu\text{m}$ surface brightness above adjacent background levels in $10^7\ \text{Jy sr}^{-1}$, occurring at a location near the apex of the nebula. Column 13 lists the angular diameter of the nebulae in arcseconds along a chord (ℓ) intersecting the peak surface brightness, as described in the text and Figure 1 of Kobulnicky et al. (2018). Column 14 lists the source of spectral classification: “O” for optical spectroscopy from APO, “I” for infrared spectroscopy from APO, “C” for optical spectra from W. T. Chick et al. (2019, in preparation), and “L” for literature spectral classifications. Column 15 lists the ratio of stellar to infrared nebular luminosity, L_*/L_{IR} , calculated from the stellar parameters, distance, and infrared measurements from Kobulnicky et al. (2017).

Figure 4 is a histogram of the ratio parallax:uncertainty for the 394 candidate bow shock stars with entries in the GDR2 (gray shaded histogram). Some GDR2 entries list negative parallaxes and are not shown. Figure 4 illustrates that the majority of bow shock candidate stars have parallax data that are (at present) insufficiently precise for reliable distance and proper motion calculation. The black shaded histogram shows the 70 stars having known spectral types, $70\ \mu\text{m}$ detections, and at least a 3:1 parallax:uncertainty ratio. Thus, the typical star retained for analysis has a distance known to 15% or better, which will reduce the uncertainties on \dot{M} compared to those presented in Kobulnicky et al. (2018).

Figure 5 presents a histogram of the projected standoff distances, R_0 , in parsec, for objects with well-determined distances and secure $70\ \mu\text{m}$ detections. The largest bow shock nebulae have characteristic sizes up to 0.6 pc, while 0.1–0.3 pc is typical. The smallest bins are incomplete because of the angular resolution limit of the SST images. We expect that a $24\ \mu\text{m}$ survey with arcsecond or better angular resolution would detect many additional arcuate nebulae, including objects at greater distances and objects with smaller standoff distances.

After distances, peculiar velocity, defined as the deviation from the star’s own local standard of rest, is the next most critical parameter. Proper motion, radial velocity, and distance, used in conjunction with a model for Galactic rotation, are sufficient to calculate the velocity of the star relative to its own

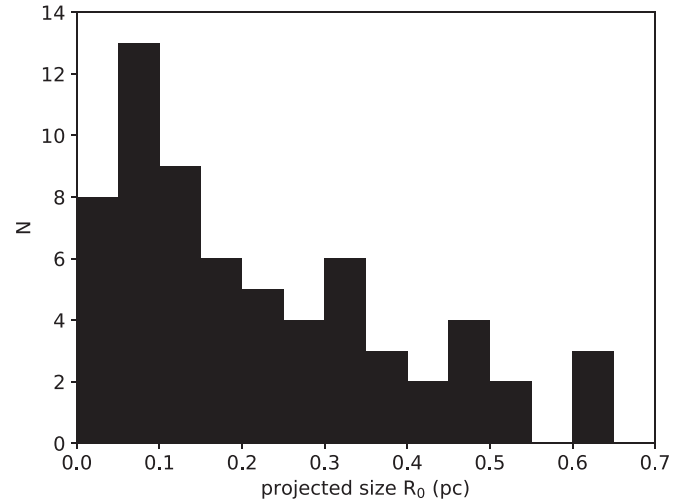


Figure 5. Histogram of the projected standoff distances, R_0 , in parsec for the 70 objects with well-determined distances and secure $70\ \mu\text{m}$ nebular detections. The lowest bin is highly incomplete owing to the angular resolution limit of the SST and WISE observatories.

local standard of rest. Ideally, precise radial velocity measurements would be available for each star. Unfortunately, the radial velocity uncertainties on most of the objects are appreciable, a consequence of calibration and random errors totaling $6\text{--}12\ \text{km s}^{-1}$. An even larger source of uncertainty is binarity. At least 50% of massive stars are found in binary systems where orbital velocities frequently exceed $100\ \text{km s}^{-1}$ (Kobulnicky et al. 2014). In order to prevent these sources of noise from dominating our estimate of peculiar velocities, we make the simplifying assumption that the stars’ velocity vectors are primarily in the plane of the sky. This is justified on the basis of the distinctive bow shock morphologies which would not be evident otherwise. Accordingly, we set the radial velocity component of each star to zero in its local standard of rest and compute the peculiar velocities solely from the two orthogonal components inferred from GDR2 proper motions.⁹ The reported peculiar velocities are, then, lower limits, but within 22% (i.e., $\sqrt{3}/\sqrt{2}$) of those expected in the case of isotropic three-dimensional velocities.

When computing peculiar velocities, we apply the matrix transformation equations of Johnson & Soderblom (1987; also see Appendix A of Randall et al. 2015 for implementation). These transformations were applied assuming Galactic center coordinates $\alpha_{\text{GC}} = 17^{\text{h}}:45^{\text{m}}:37^{\text{s}}.224$, $\delta_{\text{GC}} = -28^{\circ}:56^{\text{m}}:10^{\text{s}}.23$ and Galactic north pole coordinates $\alpha_{\text{GNP}} = 12^{\text{h}}:51^{\text{m}}:26^{\text{s}}.282$, $\delta_{\text{GNP}} = 27^{\circ}:07^{\text{m}}:42^{\text{s}}.01$ (Reid & Brunthaler 2004). We adopt a solar galactocentric distance of 8.4 kpc and the solar peculiar motion relative to the local standard of rest of $(U, V, W)_{\odot} = (11.1, 12.2, 7.2)\ \text{km s}^{-1}$ (Schönrich et al. 2010). We adopt the Milky Way rotation curve of Irigang et al. (2013, Model I). Our code for calculating peculiar velocities for bow shock stars uses the position, parallax, and proper motion for each star; removes the peculiar solar motion $(U, V, W)_{\odot}$; computes the expected $(U, V, W)_*$ for the star’s Galactic position given the adopted rotation curve; and computes the peculiar $(U, V, W)_{\text{pec}}$ velocity of the star, i.e., the star’s velocity relative to its local standard of rest. Our code reproduces the velocities of over 1000 K–M dwarf stars

⁹ The one exception is $\zeta\ \text{Oph}$, for which we use the superior data from *Hipparcos* (Perryman et al. 1997).

Table 2
Kinematic Data for Bow Shock Stars

ID	Name	GDR2 ID	V_{\odot} (km s^{-1})	Parallax (μas)	σ (μas)	μ_{α} ($\mu\text{as yr}^{-1}$)	σ ($\mu\text{as yr}^{-1}$)	μ_{δ} ($\mu\text{as yr}^{-1}$)	σ ($\mu\text{as yr}^{-1}$)
(1)	(2)	(3)	(4)	(5)	(6)	(7)	(8)	(9)	(10)
1	G000.1169−00.5703	4057291747277127040	−15	389	60	1394	94	−1045	73
3	G001.0563−00.1499	4057634103373474560	−27	640	84	−2334	135	−12128	109
7	G003.8417−01.0440	4064254301560852352	0	736	47	2020	84	−1929	67
11	G005.5941+00.7335	4067804899497964416	18	385	58	48	111	1490	85
13	G006.2812+23.5877	4337352305315545088	−9	8910	200	15260	260	24790	220
16	G006.8933+00.0743	4069437463777653632	−24	307	65	139	90	−949	74
26	G011.0709−00.5437	4094704481502396288	−1	298	42	358	78	−888	64
28	G011.6548+00.4943	4095751942430811776	−27	390	61	−820	91	−2544	78
32	G012.3407−00.3949	4095629759211238400	32	394	79	−887	104	−2037	85
46	G014.4703−00.6427	4097416946633635584	−17	1486	244	−4522	416	−1792	406
67	G017.0826+00.9744	4146617819936287488	9	638	49	−16	83	−1329	72
83	G019.8107+00.0965	4153376178622946560	0	340	38	−965	69	−2156	62
100	G023.0958+00.4411	4156581976571298944	15	526	63	67	99	−2455	93
101	G023.1100+00.5458	4156594925877520512	14	404	66	455	116	−2257	102
129	G027.3338+00.1784	4256681923166288640	−25	1130	93	1277	169	−755	130
163	G031.9308+00.2676	4266110686393370112	71	187	37	−2065	60	−4389	54
201	G037.2933+00.6703	4281150081268339072	18	926	183	−974	296	−3618	262
289	G055.5792+00.6749	2017772886883963392	18	441	48	−3204	55	−4618	67
320	G073.6200+01.8522	2059236196250413696	−4	371	35	−2567	52	−4979	65
322	G074.3117+01.0041	2060507437839909248	−15	190	27	−3163	40	−4980	44
329	G077.0505−00.6094	2063868163830050176	−39	441	54	−3802	87	−8341	97
331	G078.2869+00.7780	2067267299727875584	−51	598	42	−3330	60	−5313	60
333	G078.5197+01.0652	2067382031192434816	−12	617	84	−3072	134	−4506	159
338	G079.8223+00.0959	2064738049323468928	−10	526	61	−2357	103	−4400	116
339	G080.2400+00.1354	2064838375463800448	−43	557	40	4768	66	2509	74
341	G080.8621+00.9749	2067963015711183744	−38	587	29	−2112	51	−3843	46
342	G080.9020+00.9828	2067963535403817728	−17	621	40	−3143	69	−3058	68
344	G082.4100+02.3254	2069819545390584192	...	606	30	−2619	50	834	52
353	G104.3447+02.2299	2201205412482296448	−76	224	27	−6110	45	−1240	46
356	G106.6327+00.3917	2008430237808841600	−91	358	31	−2725	46	−1841	47
357	G106.6375+00.3783	2008383302396655488	−108	642	31	−3827	48	−1691	47
361	G108.9891+01.5606	2206818556775783552	−53	224	30	−1875	42	−981	39
362	G109.1157+00.6799	2014562519088745344	−33	148	30	−1620	53	−1386	42
367	G133.1567+00.0432	507686819685070208	52	440	26	−750	29	−279	49
368	G134.3552+00.8182	465523778576137600	−1	406	32	−1341	34	−553	52
369	G137.4203+01.2792	464697873547937664	−49	331	47	−142	53	−299	76
380	G223.7092−01.9008	3046530911350220416	21	7768	785	7193	1377	−7043	1206
381	G224.1685−00.7784	3046582725837564800	57	855	80	−2055	142	2645	169
382	G224.7096−01.7938	3046209987096803584	31	1070	350	−3140	720	3320	550
384	G253.7104−00.1920	5543183649492723584	...	232	28	−2813	40	3273	44
391	G268.9550−01.9022	5325452481440825600	...	512	29	−5124	46	3393	45
392	G269.2089−00.9138	5326951150144920064	...	497	31	−4943	51	4739	53
394	G272.5794−01.7247	5313479796251809664	...	427	29	−1142	49	−571	53
395	G273.1192−01.9620	5311906841793959936	...	344	36	−5216	81	3597	77
397	G282.1647−00.0256	5259053730157539328	...	369	27	−7909	47	4013	45
404	G286.0498−01.6583	5255179905867530752	...	222	26	−5135	54	2393	44
405	G286.4644−00.3478	5350640192585837568	...	401	26	−7009	48	3301	46
406	G287.1148−01.0236	5254478593582508288	...	332	60	−6697	121	2400	128
407	G287.4071−00.3593	5350395383778733568	...	294	34	−5996	54	2152	55
409	G287.6131−01.1302	5254268518156437888	...	262	36	−7120	64	1870	56
410	G287.6736−01.0093	5254269961265754368	...	413	27	−6968	45	1713	44
411	G288.1505−00.5059	5338310887667141888	...	455	31	−6171	53	2147	48
413	G288.3138−01.3085	5242187050013731200	...	595	77	−7892	128	3481	119
414	G288.4263−01.2245	5242184954087251456	...	356	26	−6782	47	2264	49
463	G308.0406+00.2473	5865357598905884288	...	238	38	−6063	41	−1707	50
555	G326.7256+00.7742	5885668499206748160	...	345	49	−3667	106	−2211	94
589	G332.4863+00.8256	5935169268617561344	...	366	41	−2564	82	−2358	64
624	G340.4772−00.1528	5964264231754517504	10	252	45	−2385	89	−3248	61
626	G340.8579−00.8793	5964030074446095744	−13	436	66	−851	111	−1131	84
634	G342.3422−00.4456	5964575672745370752	−11	530	58	−295	105	−2863	89
635	G342.5873+00.1600	5964883879575434240	−26	313	73	−1166	148	−818	99
637	G342.7172−00.4361	5964678060440055296	−38	743	92	−676	203	−3872	153

Table 2
(Continued)

ID	Name	GDR2 ID	V_{\odot} (km s^{-1})	Parallax (μas)	σ (μas)	μ_{α} ($\mu\text{as yr}^{-1}$)	σ ($\mu\text{as yr}^{-1}$)	μ_{δ} ($\mu\text{as yr}^{-1}$)	σ ($\mu\text{as yr}^{-1}$)
(1)	(2)	(3)	(4)	(5)	(6)	(7)	(8)	(9)	(10)
648	G344.4658–00.5580	5965562308305643008	–24	514	113	–3205	197	–3174	157
653	G346.1388–00.2184	5966132787371809536	–21	574	38	–464	62	–3330	44
655	G346.2958+00.0744	5966890930670155520	–68	434	46	–1480	76	–2738	53
673	G349.5431–00.5952	5972791773374952192	–22	342	40	–1170	74	–2088	50
692	G353.4162+00.4482	5975945894262363776	–30	558	51	1410	85	–2094	59
694	G355.4972–00.7571	4053776191953892224	–11	743	104	170	179	–951	144
700	G356.6602+00.9209	4055297370601329024	–25	271	46	–392	71	–1478	53
709	G359.9536–00.5088	4057277728502494080	–7	299	45	767	80	–2229	61

Note. (1) Identifier from Kobulnicky et al. (2016), (2) generic identifier in Galactic coordinates, (3) GDR2 identifier, (4) heliocentric radial velocity measured or adopted, as described in the Appendix, (5) *Gaia* DR2 parallax in microarcseconds, (6) parallax uncertainty, (7) GDR2 proper motion in R.A. in microarcseconds per year, (8) uncertainty, (9) GDR2 proper motion in decl. in microarcseconds per year, (10) uncertainty.

(Sperauskas et al. 2016) to within 1.1 km s^{-1} rms. Uncertainties are propagated by Monte Carlo techniques. Table 2 lists the identification number (column 1), generic name in Galactic coordinates (column 2), GDR2 identifier (column 3), observed heliocentric radial velocity (column 4), parallax and uncertainty in microarcseconds (columns 5 and 6), observed proper motions and uncertainties in R.A. in microarcseconds per year (columns 7 and 8) and decl. in microarcseconds per year (columns 9 and 10). The radial velocities, which are certain to contain large contributions from unidentified binary orbital motion in some cases, are provided here for general interest only and are not used further in this paper. The calculated space velocities, assuming zero radial velocity components, are reported in Table 3. In 11 cases, the calculated space velocity is very small—less than 5 km s^{-1} . Given the documented bow shock morphology, the relative star–ISM velocity cannot be arbitrarily small. Such sources may be examples of “in situ” bow shocks (Povich et al. 2008; Kobulnicky et al. 2016) caused by a bulk flow of ISM material. We arbitrarily impose a minimum velocity of 5 km s^{-1} for these 11 objects.

Figure 6 is a histogram of the stellar peculiar velocities, V_{tot} . Velocities range from near zero to 78 km s^{-1} . The mean and median peculiar velocities for the 70 sample objects is 15 and 11 km s^{-1} , respectively. There are no extreme-velocity stars in the sample, which is not surprising because such stars are not expected to produce visible bow shocks (Meyer et al. 2016). The mean peculiar velocity of 30 km s^{-1} assumed by Kobulnicky et al. (2018), is, in retrospect, overly large. However, there is a large dispersion of 16 km s^{-1} , so knowledge of each star’s individual peculiar velocity is important in the computation of mass-loss rates, given the V_a^2 dependence. Figure 6 also reveals that the majority of bow-shock-generating stars have a peculiar velocity less than 30 km s^{-1} and would not, on this criterion, qualify as “runaway” stars. The possibility remains that some stars reside in regions of bulk ISM flows that introduce larger star–ISM relative velocities. Kobulnicky et al. (2016) noted that an appreciable fraction of bow shocks appear oriented toward a neighboring H II region where pressure gradients that instigate ionized outflows and ISM velocities exceeding 30 km s^{-1} are plausible (Bodenheimer et al. 1979; Tenorio-Tagle 1979). Figure 5 of Kobulnicky et al. (2016) shows four bow shocks oriented toward the ionizing sources in the M16 nebula. This is a good example of where bulk ISM flows may produce “in situ” bow

shocks (Povich et al. 2008) that do not require high-velocity stars.

Figure 7 is a histogram of the ratio peculiar velocity: uncertainty, where the uncertainties are obtained by Monte Carlo error propagation. The majority of stars have ratios less than 10:1. The median value for the 70 star subsample is 4.5, meaning that the typical velocity uncertainty is about 22%. Even with the new *Gaia* data, velocity uncertainties remain significant when it comes to computing mass-loss rates, given the V_a^2 dependence.

3.1. Computation of the Mass-loss Rates

Table 3 contains quantities calculated from the basic data in Tables 1 and 2. Columns 1–4 contain the identifying numeral, name, generic name, and spectral type, as in Table 1. Column 5 contains the stellar luminosity in units of 10^4 solar luminosities computed straightforwardly from the assigned effective temperature and radius. Column 6 contains the radiation density parameter, U , calculated from the basic stellar effective temperature, radius, and standoff distance. Column 7 lists the corresponding scaled $70 \mu\text{m}$ dust emission coefficient interpolated from DL07.¹⁰ Column 8 is the factor by which the dust emission coefficients in Column 7 have been scaled from their original DL07 values, per Figure 1. Column 9 is the ambient interstellar number density, n_a , derived from the $70 \mu\text{m}$ specific intensity; the bow shock cord length, ℓ ; and the adopted j_ν , as described by Kobulnicky et al. (2018, Equation (5)). Densities range between 4 and 2100 cm^{-3} , with a median value of 20 cm^{-3} . These are typical of densities within the cool neutral phase ($\approx 30 \text{ cm}^{-3}$) and the diffuse molecular phase ($\approx 100 \text{ cm}^{-3}$) of the ISM and much larger than the warm neutral phase ($\approx 0.6 \text{ cm}^{-3}$; see Draine 2011, Table 1.3). Column 10 lists the peculiar velocity, V_{tot} , of the star derived from the proper motions, ignoring the radial velocity component. Column 11 gives its uncertainty. We caution that this velocity is only the best attempt at measuring the velocity of the star relative to its local ISM. This velocity does not account

¹⁰ We use a quadratic fit, $\log j_\nu = -0.066 \log[U]^2 + 1.07 \log[U] - 14.19$, which is valid over the range $\log U = 1.5$ – 5.0 , and is superior to the linear interpolation used by Kobulnicky et al. (2018), leading to slightly smaller emission coefficients in most cases. From the DL07 models, in $10^{-13} \text{ Jy sr}^{-1} \text{ cm}^2 \text{ nucleon}^{-1}$. We use the models for Milky Way dust in the HSO $70 \mu\text{m}$ band with the minimum PAH contribution ($q_{\text{PAH}} = 0.47\%$) and single radiation density parameter ($U_{\text{min}} = U_{\text{max}}$) as suggested by the SED analysis in Kobulnicky et al. (2017).

Table 3
Derived Parameters for Stars and Their Bow Shock Nebulae

ID	Name	Alt. Name	Sp.T.	Lum. ($10^4 L_{\odot}$)	U (10^2)	j_{ν} ($10^{-13} \text{ Jy sr}^{-1} \text{ cm}^2$)	f_j	n_a (cm^{-3})	V_{tot} (km s^{-1})	$\sigma_{V_{\text{tot}}}$ (km s^{-1})	\dot{M} ($10^{-10} M_{\odot} \text{ yr}^{-1}$)	σ ($10^{-10} M_{\odot} \text{ yr}^{-1}$)	$\Delta \log(\dot{M})$
(1)	(2)	(3)	(4)	(5)	(6)	(7)	(8)	(9)	(10)	(11)	(12)	(13)	(14)
1	...	G000.1169−00.5703	O8V	12.0	16	73	2.03	41	16.3	3.8	2639	1109	0.06
3	...	G001.0563−00.1499	B5III:	0.28	18	76	2.02	530	75.6	14.3	62957	33928	4.04
7	...	G003.8417−01.0440	B2V	0.46	20	81	1.99	453	12.1	1.3	1411	587	2.03
11	...	G005.5941+00.7335	B0V	3.4	56	135	1.8	7	31.5	3.8	201	88	0.19
13	Zeta Oph	G006.2812+23.5877	O9.2IV	4.2	21	83	1.98	9	11.9	0.1	117	45	−0.31
16	...	G006.8933+00.0743	B0III	14.0	10	57	2.15	37	5.0	3.2	673	319	−0.56
26	...	G011.0709−00.5437	O9V	5.1	46	123	1.84	17	8.2	2.5	67	27	−0.79
28	...	G011.6548+00.4943	B0V	3.4	39	114	1.86	9	15.8	4.4	96	38	−0.14
32	...	G012.3407−00.3949	B2V+B2V	0.46	8	49	2.21	73	11.5	4.7	227	98	1.23
46	...	G014.4703−00.6427	B2V:	0.46	25	91	1.95	33	17.5	3.9	169	77	1.11
67	NGC 6611ESL45	G017.0826+00.9744	O9V	5.1	229	255	1.63	163	5.5	0.9	56	25	−0.87
83	...	G019.8107+00.0965	B8II	0.29	7	46	2.25	63	9.3	1.4	208	129	2.28
100	...	G023.0958+00.4411	B1V	1.6	63	143	1.79	23	5.0	1.9	12	5	−1.19
101	...	G023.1100+00.5458	B0V	3.4	22	85	1.98	51	9.0	3.7	352	160	0.43
129	TYC 5121-625-1	G027.3338+00.1784	M0III	0.029	1	19	2.68	2111	11.3	1.2
163	...	G031.9308+00.2676	B3II	0.88	1	14	2.85	51	18.2	9.8	15376	8977	2.68
201	...	G037.2933+00.6703	B2V	0.46	38	112	1.87	40	5.0	2.7	9	4	−0.13
289	...	G055.5792+00.6749	M0III	0.029	0	0	4.48	981	16.6	1.2
320	HD 191611	G073.6200+01.8522	O9III	14.0	10	56	2.15	31	5.0	1.3	548	195	−0.66
322	...	G074.3117+01.0041	O8IV:	19.0	14	68	2.07	14	11.4	2.4	754	306	−0.80
329	KGK 2010-10	G077.0505−00.6094	O8V	7.9	101	177	1.72	11	41.6	5.2	474	185	−0.32
331	LSII+39 53	G078.2869+00.7780	O7V	12.0	15	70	2.06	14	12.9	0.7	471	206	−0.69
333	...	G078.5197+01.0652	B0V+B0V	4.4	12	62	2.11	74	8.8	1.6	270	109	−0.03
338	CPR 2002A10	G079.8223+00.0959	O8V:	7.9	26	93	1.94	114	5.0	1.8	282	115	−0.54
339	CPR 2002A37	G080.2400+00.1354	O5V	32.0	12	63	2.1	35	78.1	6.6	121619	49228	0.90
341	KGK 2010-1	G080.8621+00.9749	O9V	5.1	27	95	1.93	8	5.0	0.8	17	6	−1.39
342	KGK 2010-2	G080.9020+00.9828	B4V	0.093	2	23	2.59	795	12.2	1.1	4115	2115	3.86
344	BD+43 3654	G082.4100+02.3254	O4If	87.0	5	39	2.33	39	37.7	2.3	197923	72806	0.42
353	...	G104.3447+02.2299	O5V	32.0	12	63	2.1	7	65.2	7.9	17007	6931	0.05
356	HD 240015	G106.6327+00.3917	B0III	14.0	49	127	1.83	5	5.0	1.0	22	9	−2.05
357	HD 240016	G106.6375+00.3783	B2III	3.8	20	81	1.99	8	13.5	0.5	245	93	−0.41
361	TYC 4278-522-1	G108.9891+01.5606	B1Ia	8.7	0	7	3.25	12	19.2	2.1	76045	45397	1.43
362	...	G109.1157+00.6799	B2I	13.0	12	63	2.1	4	22.4	3.6	1608	721	−0.62
367	LSI+60 226	G133.1567+00.0432	O7V	12.0	11	61	2.12	8	5.0	1.0	50	20	−1.66
368	KM Cass	G134.3552+00.8182	O8.5V	7.0	39	113	1.87	31	5.4	1.3	53	22	−1.12
369	BD+60 586	G137.4203+01.2792	O8III	19.0	2	25	2.54	20	8.4	3.1	3278	1549	−0.17
380	HD 53367	G223.7092−01.9008	B2Ve:	0.46	322	297	1.6	131	10.7	1.5	20	7	0.46
381	HD 54662	G224.1685−00.7784	O7Vz	12.0	1	14	2.84	10	6.8	1.5	1287	530	−0.25
382	FN Cma	G224.7096−01.7938	B0III	12.0	7	48	2.22	25	9.1	5.2	1764	1968	0.07
384	CD-35 4415	G253.7104−00.1920	O7III _{nn}	26.0	10	58	2.14	32	5.1	3.2	530	203	−1.25
391	HD 77207	G268.9550−01.9022	B7Iab +	3.2	5	38	2.33	15	11.2	1.1	1538	940	0.85
392	CPD-47 3051	G269.2089−00.9138	B0V	3.4	6	45	2.26	12	5.0	1.2	77	33	−0.23
394	HD 298310	G272.5794−01.7247	B0V	14.0	37	111	1.87	5	67.0	4.1	3914	1446	0.20
395	HD 298353	G273.1192−01.9620	O7V	12.0	9	54	2.17	18	10.1	2.7	604	271	−0.58
397	CD-55 3196	G282.1647−00.0256	O9.5III	13.0	24	89	1.96	28	23.2	2.9	4378	1787	0.28
404	CD-59 3123	G286.0498−01.6583	O9.5Ib	30.0	3	31	2.43	7	24.4	6.4	16560	7927	0.37

Table 3
(Continued)

ID	Name	Alt. Name	Sp.T.	Lum. ($10^4 L_\odot$)	U (10^2)	j_ν (10^{-13} Jy sr $^{-1}$ cm 2)	f_j	n_a (cm $^{-3}$)	V_{tot} (km s $^{-1}$)	$\sigma_{V_{\text{tot}}}$ (km s $^{-1}$)	\dot{M} ($10^{-10} M_\odot$ yr $^{-1}$)	σ ($10^{-10} M_\odot$ yr $^{-1}$)	$\Delta \log(\dot{M})$
(1)	(2)	(3)	(4)	(5)	(6)	(7)	(8)	(9)	(10)	(11)	(12)	(13)	(14)
405	HD 303197	G286.4644−00.3478	B3III	0.88	2	22	2.61	62	7.7	1.5	1706	821	1.72
406	HD 92607	G287.1148−01.0236	O9IVn	8.2	24	88	1.96	32	7.9	4.9	338	126	−0.46
407	HD 93249	G287.4071−00.3593	O9III+O	14.0	141	207	1.68	26	9.1	2.1	109	43	−1.37
409	HD 93027	G287.6131−01.1302	O9.5IV	4.0	36	108	1.88	23	22.1	5.2	693	284	0.44
410	HD 305536	G287.6736−01.0093	O9.5V+ B	4.1	338	302	1.6	66	11.6	1.6	30	11	−0.95
411	HD 305599	G288.1505−00.5059	O9.5V	4.1	314	294	1.61	79	6.8	1.0	26	11	−1.01
413	HD 93683	G288.3138−01.3085	O9V+B0V	5.1	49	126	1.83	19	9.2	3.5	41	16	−1.00
414	HD 93858	G288.4263−01.2245	B3II	0.88	22	85	1.98	16	6.0	1.6	25	12	−0.11
463	TYC 8995-1548-1	G308.0406+00.2473	B0III:	12.0	20	80	2.0	9	5.0	2.7	67	27	−1.35
555	ALS 18049	G326.7256+00.7742	O9V:	5.1	243	263	1.63	82	13.0	2.2	150	57	−0.44
589	CD-49 10393	G332.4863+00.8256	B0V	3.4	33	105	1.89	10	7.4	1.5	27	11	−0.67
624	...	G340.4772−00.1528	B0III	14.0	19	78	2.01	9	27.4	5.0	2496	1039	0.01
626	...	G340.8579−00.8793	O9V	5.1	47	124	1.83	187	12.8	1.5	1717	645	0.62
634	HD 152756	G342.3422−00.4456	B0III	12.0	20	82	1.99	10	5.9	2.4	101	42	−1.17
635	...	G342.5873+00.1600	O6V	19.0	11	59	2.13	20	16.7	3.7	2244	1458	−0.38
637	...	G342.7172−00.4361	B2V	0.46	45	121	1.84	13	5.0	3.5	3	1	−0.63
648	...	G344.4658−00.5580	B0III	14.0	102	177	1.72	8	23.7	10.7	339	130	−0.86
653	...	G346.1388−00.2184	K0III:	0.005	2	26	2.51	87	7.4	1.6
655	...	G346.2958+00.0744	B1V:	1.6	163	221	1.66	19	12.3	3.0	23	9	−0.91
673	...	G349.5431−00.5952	B1V:	1.6	35	107	1.88	10	12.9	3.1	59	23	−0.5
692	...	G353.4162+00.4482	O7V	12.0	20	81	2.0	116	13.6	2.2	3416	1638	0.17
694	...	G355.4972−00.7571	B2V:	0.49	46	124	1.83	17	9.5	1.8	14	7	−0.03
700	...	G356.6602+00.9209	B0V	3.4	6	45	2.26	8	9.5	4.8	180	84	0.14
709	...	G359.9536−00.5088	B0V+B1V	3.4	16	72	2.04	12	21.5	6.0	317	127	0.38

Note. (1) Identifier from Kobulnicky et al. (2016), (2) common name, (3) generic identifier in Galactic coordinates, (4) spectral classification, (5) stellar luminosity in units of 10^4 times the solar luminosity, computed from the effective temperature and radius in Table 1, (6) dimensionless ratio of the radiant energy density (in erg cm $^{-3}$) from the star to the mean interstellar radiant energy density estimated by Mathis et al. (1983, MMP83) (7) dust emission coefficient in 10^{-13} Jy sr $^{-1}$ cm 2 per nucleon, following DL07, after scaling by the factor f_j , (8) scale factor, f_j , for dust emission coefficients on account of the harder radiation field near OB stars, as described in the text, (9) computed ambient interstellar number density, following Equation (5) of Kobulnicky et al. (2018), (10) peculiar velocity in the star's local standard of rest; an arbitrary minimum of 5 km s $^{-1}$ has been imposed. Velocities include only the two plane-of-sky components and not the radial component, as discussed in the text. (11) Peculiar velocity uncertainty, (12) computed mass-loss rate in 10^{-10} solar masses per year, (13) uncertainty on the mass-loss rate. Uncertainties do not include the uncertainties on the star's peculiar velocity and, hence, are lower limits, (14) the base 10 logarithm of our derived mass-loss rate minus the logarithm of the theoretical Vink et al. (2001) mass-loss rate, after correcting the theoretical values downward by 0.12 dex on account of the revision to the solar abundance scale since that work. For G012.3407−00.3949, G078.5197+01.0652, G287.4071−00.3593, G288.3138−01.3085, and G359.9536−00.5088, we have divided the mass-loss rate by a factor of 2 in order to account for the double nature of these sources. There are certain to be other unidentified binaries among our sample.

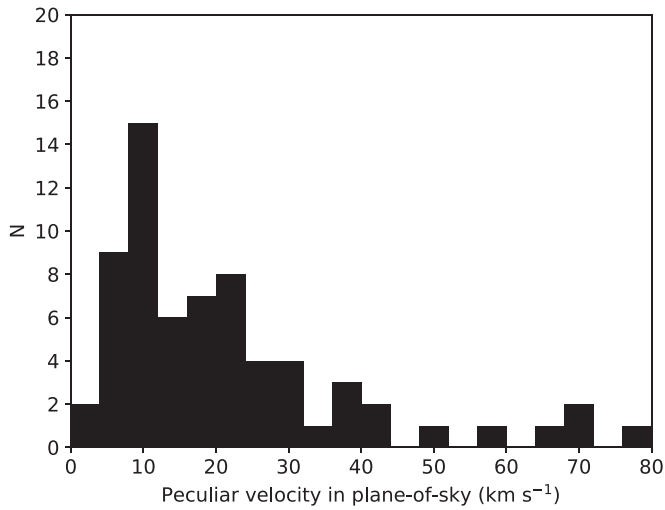


Figure 6. Histogram of stellar peculiar velocities relative to their local rest frame. The histogram depicts the 70 stars selected for analysis.

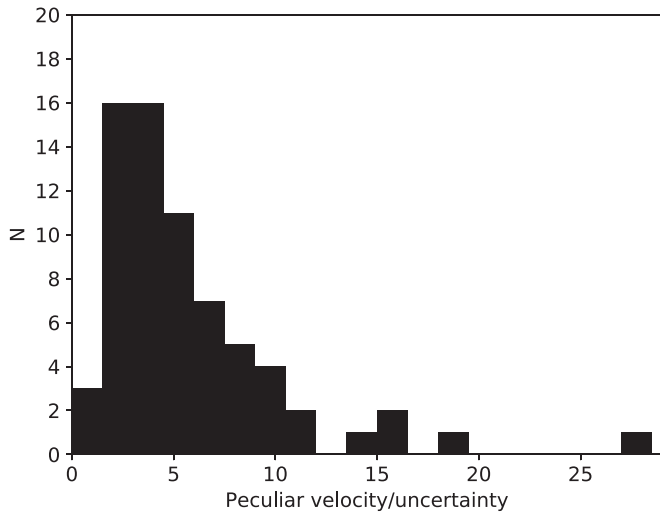


Figure 7. Histogram of the ratio peculiar velocity:uncertainty. The histogram depicts the 70 stars selected for analysis.

for the possibility of local bulk flows of interstellar material, such as “champagne flows” from expanding H II regions. Columns 12 and 13 contain the mass-loss rates and corresponding uncertainties calculated from Equation (2). Values range from $6 \times 10^{-10} M_{\odot} \text{ yr}^{-1}$ to $5 \times 10^{-5} M_{\odot} \text{ yr}^{-1}$. Column 14 lists the difference between the logarithm of our derived mass-loss rate and the logarithm of the theoretical mass-loss rate, calculated using Equations (24) and (25) of Vink et al. (2001).

In Kobulnicky et al. (2018), we assessed the uncertainties on \dot{M} in terms of the uncertainties on each measurable parameter in Equation (2). The angular quantities R_0 and ℓ are measured to about 10% from infrared images, unchanged from our earlier work. I_{ν} is measured to about 20%, probably worse for some of the faintest nebulae. Mean stellar-wind velocities are also unchanged, accurate to 30% and showing real variation from star to star (e.g., Mokiem et al. 2007). Similarly, the uncertainty on j_{ν} is driven by the uncertainties on stellar temperature (taken to be 2000 K), radius (10%), and standoff distance (we use the actual tabulated uncertainties); however, systematic uncertainties on the absolute values may exist at the 60% level. Stellar

distances and velocities—previously the dominant sources of uncertainty—are now known much more precisely by virtue of the new *Gaia* data, but they still have significant uncertainties as shown in Figures 4 and 6 and by the data in Table 3. We calculate uncertainties on the mass-loss rates using a 1000 iteration Monte Carlo error propagation procedure with the aforementioned uncertainties as inputs. Our procedure would ideally start with the basic *Gaia* parallax and proper motion measurements for a proper ab initio error analysis. However, because we lack access to the Bailer-Jones et al. (2018) Bayesian code, we adopt the nominal distances and uncertainties from that work as well as the nominal stellar peculiar velocities and uncertainties they imply in order to further propagate the uncertainties from the stellar temperature, radius, wind speed, and nebula angular quantities from Equation (2). We find that a significant fraction of the iterations would result in unphysical negative peculiar velocities if the nominal velocity errors were used, e.g., 2 ± 1 yields a non-negligible fraction of negative values. This, combined with the likelihood that bulk ISM flows are an appreciable component of the star–ISM relative velocity, leads us to exclude velocity uncertainties from the Monte Carlo error analysis. Therefore, the ensuing uncertainties on \dot{M} appearing in the last column of Table 3 should be regarded as indicative of lower bounds. The average uncertainty is 42% (excluding uncertainties on dust emission coefficients and stellar peculiar velocities).

4. Analysis

4.1. Presentation of Mass-loss Rates

Figure 8 plots the calculated mass-loss rates versus stellar effective temperature.¹¹ Black filled symbols denote the sample objects: a star for ζ Oph, filled circles for luminosity class V and IV stars, and open circles for giants and supergiants. A small dispersion has been added to the data points along the temperature axis to prevent marker pile-up. Green circles enclose the objects where the peculiar velocities were set to the minimum value of 5 km s^{-1} . Not surprisingly, these lie near the lower edge of the distribution. Orange circles mark the objects having $L_{*}/L_{\text{IR}} < 75$ as potential radiation bow waves. This criterion was selected based on the principles outlined in Henney & Arthur (2019) and after some experimentation that showed this cutoff selects all of the low-temperature stars with excessively large implied mass-loss rates but only a few of the hotter stars. Two mid to late B stars from Table 3 lie off the left side of this plot, as do the three cool late-type (K–M) stars. Blue crosses depict model predictions for each object using the formulation of Vink et al. (2001, Equations (24) and (25))¹² computed using the stellar data from Table 1.¹³ We assume $v_{\infty}/v_{\text{esc}} = 2$ for stars on the hot side of the bistability jump and 1.3 for the cool side, per Vink et al. (2001). Hence, each filled

¹¹ Although the mass-loss rate is expected to scale with luminosity rather than temperature (and to a lesser extent, metallicity; we only consider solar metallicities), we choose to plot the latter to facilitate direct comparison with the Lucy (2010) models.

¹² We use the former for objects hotter than 27,000 K and the latter for cooler stars, given that we are unable to distinguish the correct branch for objects in the 22,500–27,000 K transition regime.

¹³ The downward revision of the solar metal abundance scale by Asplund et al. (2005) relative to the older Anders & Grevesse (1989) scale used by prior works including Vink et al. (2001) would result in a predicted mass-loss rate lower by about 0.12 dex (Krtićka & Kubát 2007). We have, accordingly, lowered all of the pre-2005 theoretical predictions by this amount throughout this work. The correction is small compared to the dispersion in the data.

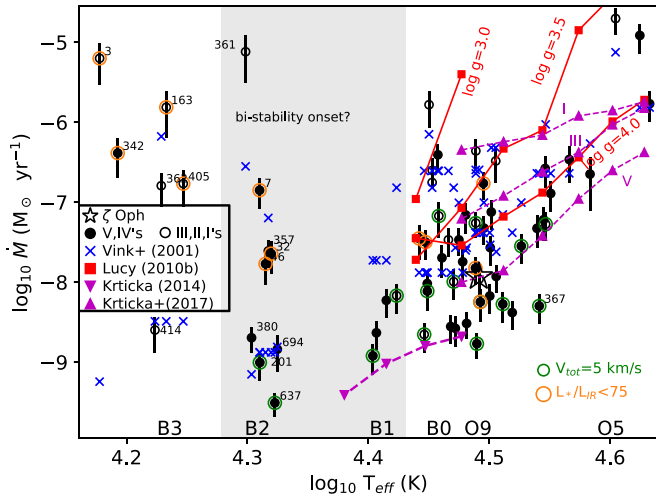


Figure 8. Mass-loss rate vs. stellar effective temperature. Black filled points and black open circles depict measurements for main-sequence and evolved stars from this sample, respectively. Blue crosses mark the predictions for each object using the expressions of Vink et al. (2001, Equations (24) and (25)). Red squares and lines show the model predictions of Lucy (2010) for nominal main-sequence ($\log g = 4.0$), giant ($\log g = 3.5$), and supergiant ($\log g = 3.0$) stars, as labeled. The triangles and dotted lines show the theoretical predictions of Krtićka (2014) and Krtićka & Kubát (2017) for B and O stars, respectively. Green circles identify stars where the stellar peculiar velocity, v_{tot} , has been arbitrarily fixed to the minimum values of 5 km s^{-1} . Orange circles enclose objects that are candidate radiation bow wave nebulae. Two evolved B stars from Table 3 lie off the left side of this plot, as do the three cool late-type stars. A gray band marks the expected region of the bistability phenomenon.

data point is paired vertically with a blue \times at the same temperature, although the \times 's sometimes overlap. Red squares connected by lines depict the model predictions from Lucy (2010) for (approximate) main-sequence ($\log g = 4.0$), giant ($\log g = 3.5$), and supergiant ($\log g = 3.0$) stars, as labeled. Magenta triangles and dashed lines show the predictions for B main-sequence stars from Krtićka (2014, solar abundance models) and O stars (Krtićka & Kubát 2017), with separate tracks for stellar luminosity classes I, III, and V. A gray band marks the predicted regime of the bistability jump.

For the hot portion of the sample, the data show mass-loss rates rising from a few $\times 10^{-9} M_{\odot} \text{ yr}^{-1}$ near 27,000 K to over $10^{-6} M_{\odot} \text{ yr}^{-1}$ for O5 stars near 42,000 K, but with a large dispersion of about half an order of magnitude. The data points for stars B1 and earlier fall systematically below the Lucy (2010) and Vink et al. (2001) predictions, but broadly consistent with—if slightly above—the Krtićka (2014) and Krtićka & Kubát (2017) models. The results are similar to those of Kobulnicky et al. (2018) but for a sample more than three times as large extending to cooler temperatures. The dispersion of the data is larger than the typical uncertainties in the vertical dimension, consistent with additional uncertainty terms and/or real variations. Considering the ± 1 subtype uncertainty on classifying any particular star, especially early B stars, any given object may fall into an adjacent temperature bin. Evolved stars (open circles) generally lie above the luminosity class V and IV stars, also in accordance with model predictions.

The prototypical bow shock star ζ Oph, in particular, shows good agreement with the Krtićka & Kubát (2017) models. With $L_{*}/L_{\text{IR}} = 1700$, ζ Oph is safely out of the dust bow wave regime and should represent a good point of reference for studies employing other techniques. Our nominal derived \dot{M} of $1.2 \times 10^{-8} M_{\odot} \text{ yr}^{-1}$ is a factor of 15 lower than the estimate of

$1.8 \times 10^{-7} M_{\odot} \text{ yr}^{-1}$ from Repolust et al. (2004), which assumed no wind clumping correction, and hence, must be regarded as an upper limit. Had we included the radial velocity component of ζ Oph's total space velocity (as one of the stars where the assumption of zero radial velocity is known to be inconsistent with the data), the resulting space velocity of 26 km s^{-1} would imply a mass-loss rate of $5.5 \times 10^{-8} M_{\odot} \text{ yr}^{-1}$, still considerably lower than Repolust et al. (2004), but only by a factor of 3, which would be consistent with a standard correction for wind clumping. Differences in the adopted stellar parameters ($v_{\infty} = 1550$, $R_{*} = 8.9 R_{\odot}$, $T_{\text{eff}} = 32,000 \text{ K}$ versus the $1300/7.2 R_{\odot}/31,000 \text{ K}$ adopted here) are relatively minor effects. Repolust et al. (2004) note that this star is a rapid rotator with $V_r \sin i = 400 \text{ km s}^{-1}$, which could induce non-isotropic winds and modify the published values in either observational or theoretical analyses, or both. Our derived mass-loss rate for ζ Oph is still a factor of 10 or more larger than the $\dot{M} = 1.5 \times 10^{-9} M_{\odot} \text{ yr}^{-1}$ inferred from an analysis of X-ray line profiles (Cohen et al. 2014) or the $1.6 \times 10^{-9} M_{\odot} \text{ yr}^{-1}$ from UV absorption lines (Marcolino et al. 2009). Hence, there remains a considerable discrepancy between observational results on this prototypical “weak wind” late O star.

B1 and later spectral types in Figure 8 fall considerably above the Krtićka (2014) prediction and above an extrapolation of the Lucy (2010) models. These stars lie within the predicted regime of the bistability discontinuity. They show a large dispersion in mass-loss rates from $<10^{-9} M_{\odot} \text{ yr}^{-1}$ to almost $5 \times 10^{-5} M_{\odot} \text{ yr}^{-1}$, approaching—but not exceeding—the very large mass-loss rates predicted by Vink (2018) for LBV stars, in a few instances. Notably, a majority of the stars in this regime are candidates for being dust bow wave objects, having $L_{*}/L_{\text{IR}} < 75$, making their derived mass-loss rates suspect. However, the positions of some of these stars, particularly those that are not bow wave candidates, are broadly consistent with the Vink et al. (2001) prescriptions that take into account the effects of bistability below $\approx 27,000 \text{ K}$.

Figure 9 plots the difference of the logarithms between the mass-loss rates derived in this work and those predicted by the Vink et al. (2001) formulation versus effective temperature. As before, filled markers denote (near-) main-sequence objects and open circles denote giants and supergiants. A gray band highlights the range of the expected bistability jump. Numerals adjacent to symbols identify each object, with a larger font for objects having our own optical spectroscopy and a smaller italic font for other stars. Black symbols denote comparisons performed using the Vink et al. (2001) upper/lower branch formulae for objects above/below 27,000 K, respectively. Red symbols show stars having $T_{\text{eff}} < 27,000 \text{ K}$ if the upper-branch prescription ignoring bistability effects was used instead. Green circles enclose objects where the lower limit peculiar velocity of 5 km s^{-1} was assigned. Orange circles enclose candidate bow wave objects having $L_{*}/L_{\text{IR}} < 75$. Blue squares enclose objects that directly face an $8 \mu\text{m}$ bright-rimmed cloud where photoevaporative flows from the molecular cloud interface may influence the infrared nebulae. Horizontal dashed lines mark the mean (bold dotted) and dispersion (non-bold dotted) for all points above 25,000 K. The mean lies at -0.43 dex , indicating that, on average, the mass-loss rates are a factor of 2.7 below the Vink et al. (2001) prescription in this regime, with a considerable dispersion of 0.64 dex (factor of 4). A direct comparison with the predictions

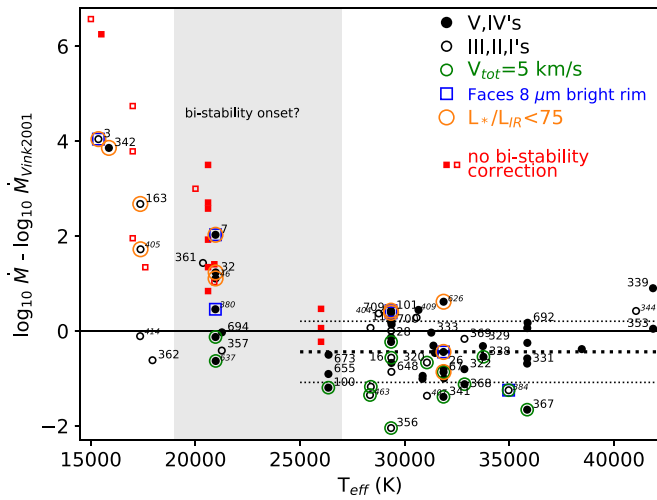


Figure 9. The log of the mass-loss rate derived in this work minus the log of the Vink et al. (2001) prescription vs. effective temperature. Numerical labels identify stars with $H\alpha$ spectra presented in Figure 10 (larger font) and other objects of interest (smaller italic font). Black symbols denote comparisons performed using the Vink et al. (2001) upper/lower branch formulae for objects above/below 27,000 K, respectively. Red symbols show stars having $T_{\text{eff}} < 27,000$ K if the upper-branch prescription neglecting bistability effects were used instead. Green circles mark objects where the lower limit peculiar velocity of 5 km s^{-1} was assigned. Orange circles enclose objects that are candidate radiation bow wave nebulae. Blue squares enclose objects that directly face an $8 \mu\text{m}$ bright-rimmed cloud.

of Krtićka & Kubát (2017) is not possible owing to the limited number of models tabulated in that work, but it may be concluded from Figure 8 that our inferred mass-loss rates lie, on average, above those values by 0.1–0.3 dex. The large dispersion in the data points in this figure results partly from the uncertainties in the derived mass-loss rate, typically 0.2–0.3 dex (see Table 3, but recall that the tabulated uncertainties here do not include errors in V_a), systematic errors on dust emission coefficients, or additional uncertainties on the computed theoretical Vink et al. (2001) mass-loss rate (driven by uncertainties on the adopted parameters including the stellar luminosity, mass, effective temperature, terminal wind speed, and metallicity), amounting to another ~ 0.2 –0.3 dex.

Figure 9 demonstrates that there is a systematic difference between our mass-loss estimates and theoretical models at temperatures $> 25,000$ K and a much larger dispersion in mass-loss rates for stars $< 25,000$ K. The agreement between data and models is better when the prescription for bistability is applied—that is, the positions of the black data points are consistent with the models minus a small offset versus the red symbols which depart dramatically from the predictions toward lower temperatures. Unfortunately, our spectra do not contain the Si II and Si III lines in the blue portion of the optical spectrum required to assign temperatures to hot stars, so we are unable to ascertain the operative temperature where this deviation begins. Realistically, enhanced mass loss may become evident over a range of temperatures and luminosities depending on other factors traditionally linked to wind strength such as the stellar mass, metallicity, and rotation rate. Indeed, Crowther et al. (2006) identified a systematic drop in terminal wind speeds across a 4000 K range in a sample of B supergiants but these authors, as well as Markova & Puls (2008), did not find a corresponding increase in mass-loss rates. Hence, our data in Figures 8 and 9 could represent the first

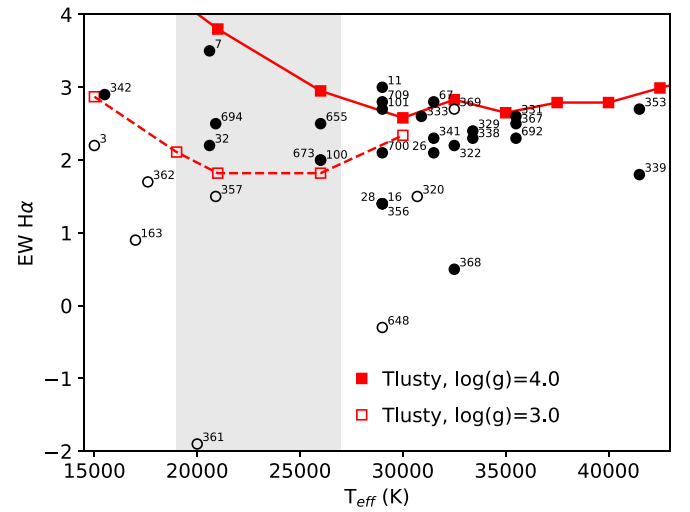


Figure 10. $H\alpha$ equivalent width vs. effective temperature for 37 stars with suitable data. The red points and lines are the expectations for dwarf and supergiant gravities from theoretical model spectra with no mass loss (Lanz & Hubeny 2003).

evidence for enhanced mass-loss associated with the bistability phenomenon. In particular, the most reliable data points (those without orange circles) show reasonable agreement with the Vink et al. (2001) predictions, falling below the horizontal line by about 0.43 dex, similar to the hotter portion of the sample. An extrapolation of the heavy dotted line marking the mean of the $T_{\text{eff}} > 25,000$ stars would intersect the most reliable B2–B3 objects in our sample, provided that the proper bistability formulation is used to predict the theoretical values. Our estimate of the mass-loss rates for these objects, $\sim 10^{-9} M_{\odot} \text{ yr}^{-1}$, for the four B2V stars represents the first results for dwarf stars in this temperature regime. Their values are, like the hotter portion of the sample, about a factor of 2.5 below the Vink et al. (2001) predictions.

If the especially high rates of mass loss for some cool objects were taken at face value, it ought to imprint an observable signature in the spectra in the form of extraphotospheric $H\alpha$ emission. While we do not have high-resolution optical spectra of the sample stars that would be required to detect low levels of emission in the line cores, we do have low-resolution spectra for 37 stars. Figure 10 plots the observed $H\alpha$ equivalent width versus stellar effective temperature for the sample stars with suitable data. Solid circles represent main-sequence stars, and open circles represent evolved stars, as in previous figures. Numerals designate each object by identification number. The red squares and lines mark theoretical values from model atmospheres (Tlusty, Lanz & Hubeny 2003, the O- and B-star grids for solar metallicity) that are appropriate to plane-parallel static atmospheres without a wind. Positive values represent absorption and negative values represent emission, per conventional usage. While the equivalent width of $H\alpha$ is expected to increase from hot to cool (simply because Balmer lines become stronger toward cooler stars in this temperature range) across the bistability region, the data are mostly flat or decreasing, consistent with seeing elevated mass loss over the 27,000–19,000 K regime. Most points in this range lie below theoretical expectations consistent with a small contribution from extraphotospheric emission. The lack of strong emission lines from the cool objects with very high implied mass-loss rates in Figure 8 suggests that the infrared nebulae in such

objects are driven by radiation pressure, not winds, consistent with their small L_*/L_{IR} ratios.

A comparison of outliers in Figures 8–10 provides a means of assessing whether mass-loss rates are internally consistent. Considering first the coolest objects at the left edge of both figures, the B4V #342 and the B5III #3 have derived mass-loss rates four orders of magnitude above the model predictions, even when bistability effects are considered. Both objects have $H\alpha$ substantially in excess of the stellar photosphere, but not in emission, as might be expected for such large mass-loss rates. While both objects have nebular surface brightnesses that are among the highest in the sample, they are not extraordinary in this regard. But they are extraordinary in that the nebular surface brightnesses are high for their late (cool!) spectral type. Both nebulae are bright at $8\mu\text{m}$, indicating PAH emission consistent with a molecular cloud interface. Furthermore, #3 faces an $8\mu\text{m}$ bright cloud rim (Kobulnicky et al. 2016, Figure 13.3) and is among the objects considered by Kobulnicky et al. (2016) to be affected by a photoevaporative flow from the inner edge of that rim. The extent of the impacts from this phenomenon has not been theoretically developed. Both #3 and #342 have $L_*/L_{\text{IR}} < 75$, making them probable radiation bow waves. Among the four evolved $\approx B3$ stars, #163 (B3II) and #405 (B3III) lie 2–3 orders of magnitudes above Vink et al. (2001) predictions while #362 (B2I) and #414 (B3II) lie close to the model predictions. $H\alpha$ for #163 lies well in excess of the model photosphere (but not in emission). This nebula lies along a $70\mu\text{m}$ filament that does not show good morphological correspondence with the $24\mu\text{m}$ nebulae. It is likely that this object is confused by unrelated foreground or background emission. In the case of #405, we do not have $H\alpha$ data. It faces the IC 2599 H II region associated with the energetic young cluster NGC 3324, which may drive an outflow and create a relative star–ISM velocity in excess of the tabulated 7.7 km s^{-1} . Both #163 and #405 are probable radiation bow wave nebulae. Objects #362 and #414, on the other hand, agree well with model predictions once bistability behavior is considered. Neither object has evidence for being an instance of the radiation bow wave phenomenon.

Stars in the B2 temperature range show mass-loss rate estimates in better agreement with model predictions, on average, but some still lie far above expectations in Figure 9. Object #7 (B2V), for example, lies two orders of magnitude above the Vink et al. (2001) predictions in Figure 9. Like #3, it is a probable radiation bow wave nebula. It faces a bright-rimmed cloud prominent at $8\mu\text{m}$ and may be affected by a photoevaporative flow (Kobulnicky et al. 2016, Figure 13.7). Examination of the mid-infrared image in Kobulnicky et al. (2016) shows another star $40''$ to the southwest of the nebulae that also lies along the nebula axis of symmetry. Identified as an AGB star candidate (Robitaille et al. 2008), 2MASS J17582964–2610138 (R.A.(2000) = $17^{\text{h}}:58^{\text{m}}:29^{\text{s}}.64$, decl.(2000) = $-26^{\circ}:10^{\text{m}}:13^{\text{s}}.8$) has $H = 10.4$ mag and $A_K = 3.08$, an implied extinction that apparently precludes its inclusion in the GDR2, so its distance is unknown. If this star is the source of the luminosity powering the nebula, it should be marked with an open circle in Figure 8 among other luminous evolved cooler stars. This object should be regarded as uncertain in all respects. Object #361 (B1Ia; highly uncertain type and luminosity class) has a $70\mu\text{m}$ nebula that is very near the detection limit, and the background is correspondingly very uncertain. The derived mass-loss rate could be considered an upper limit. Object #32 (a

probable B2V+B2V binary) lies near an extended $70\mu\text{m}$ nebulosity that makes the background level somewhat uncertain. It is also a radiation bow wave candidate. Object #46 (B2V; also a radiation bow wave candidate) has an unusually large implied reddening for its parallax distance ($D_{\text{par}} = 688_{-111}^{+163}$ pc; $A_V \simeq 11$ mag; see the Appendix), which may have implications for its nature and derived mass-loss rate. Object #380 (B2Ve) also faces a bright-rimmed cloud, a feature in common with other stars that show above-predicted mass-loss rates in Figure 9. The remaining four objects in this temperature regime (#694–B2V, #201–B2V, #357–B2III, and #637–B2V) all show mass-loss rates near the predicted values, and they all appear to be isolated objects with well-defined nebulae. These objects comprise what we believe to be the first collection of B2 dwarfs with measured mass-loss rates, although two of these have the assigned minimum peculiar velocity of 5 km s^{-1} .

The next group of three hotter stars near B1 shows improved agreement with the theoretical predictions. All three lie slightly above the Krtićka (2014) prediction in Figure 8 but substantially below the Vink et al. (2001) prediction, best visualized in Figure 9. Our data represent the first estimate of mass-loss rates for dwarfs of this temperature class.

Other outliers in Figure 9 merit some discussion. Object #101 (B0V) faces an $8\mu\text{m}$ bright-rimmed cloud and is a possible radiation bow wave with $L_*/L_{\text{IR}} < 75$. Object #626 (O9V) is also a radiation bow wave candidate, having the second highest nebular surface brightness in our sample. Object #339 (O5V) has one of the largest nebulae in our sample, and it has the largest peculiar velocity (78 km s^{-1}). It also displays a $H\alpha$ EW considerably in excess of the photosphere in Figure 10. Object #344 (the well-studied O4If star BD+43 3654) has the highest mass-loss rate in our sample ($5 \times 10^{-5} M_{\odot} \text{ yr}^{-1}$), somewhat in excess of predictions. There is the possibility that many of these objects are unrecognized binaries, and that their derived mass-loss rates should be reduced accordingly—0.3 dex for equal-luminosity components. Objects that fall far below expectations are often those where the minimum peculiar velocity of 5 km s^{-1} has been assigned. These include #356 (B0III), #463 (B0III), #341 (O9V), and #367 (O7V). One other evolved object, #407 (O9III+O), is a radiation bow wave candidate, but falls far below model expectations. Object #407 could also be an in situ type bow shock as it does face directly toward the very energetic Carina star-forming complex at an angular separation of $\approx 0.2^\circ$. As such, its peculiar velocity may underestimate its true star–ISM velocity. Conversely, object #409 (O9.5IV) lies above model predictions and also faces the Carina nebula.

4.2. An Investigation of Biases by Subsample

In an effort to investigate whether sample selection effects impact the essential conclusions from Figure 8, we considered only the half of the sample having nebular surface brightness above the median value. We found that the essential conclusions from Figure 8 are unchanged, with the O stars and early B stars showing good agreement with models and having a similar dispersion to the full sample. However, fewer of the cooler stars are retained in this cut, indicating that the majority of the high-surface-brightness nebulae are, unsurprisingly, associated with hotter stars. The lower surface brightness of the nebulae associated with the B stars in this sample means that they carry larger uncertainties, by virtue of the difficulty defining and subtracting local background emission around

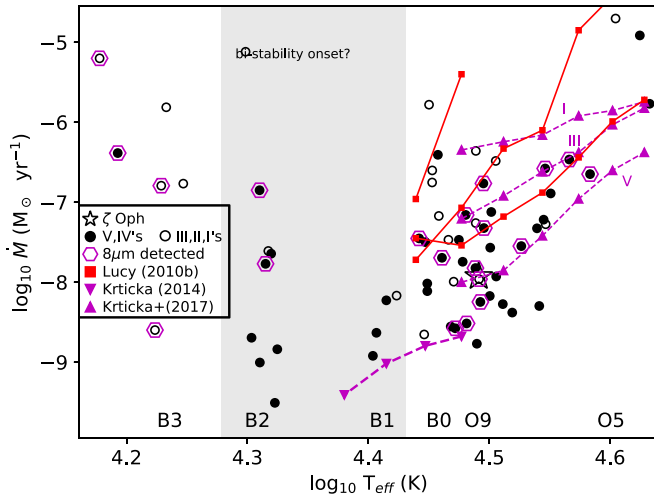


Figure 11. As in Figure 8, but now objects with $8\ \mu\text{m}$ detections, suggesting probable PAH contributions, are circled in magenta hexagons. Objects with PAH emission lie scattered throughout the parameter space, indicating no significant bias on account of PAH-emitting nebulae.

each nebula. We also replicated Figure 8 for the half of the sample having the highest velocity precision (indicated by the peculiar velocity:uncertainty ratio V_{tot}/σ_v) above the median value of 4.5. The essential elements of Figure 8 remain. O stars and early B stars show good agreement with the models and have similar dispersion as before while the cooler stars exhibit the same dispersion observed in the full sample. We conclude that including stars with larger velocity uncertainties does not bias the results in any particular direction. Figure 11 replicates the full set of objects from Figure 8, but magenta hexagons now enclose nebulae having $8\ \mu\text{m}$ detections, suggestive of possible PAH contributions. Sources with $8\ \mu\text{m}$ detections lie scattered throughout the figure, occurring both at low and high temperatures as well as at low and high mass-loss rates. However, at the cooler end of the temperature range, most of the points that fall far above the expected trend are those with PAH detections. Many among this subset are also radiation bow wave candidates. Hence, at high temperatures, the presence or absence of PAH features does not appear to bias the data in any particular direction, but at low temperatures it may be wise to treat such objects with caution.

Table 4 provides a list of object ID numbers that fall into each of the aforementioned special categories. These are the 11 objects having $V_{\text{tot}} < 5\ \text{km s}^{-1}$, the seven objects that face $8\ \mu\text{m}$ bright-rimmed clouds, and the 15 candidate bow-wave objects having $L_*/L_{\text{IR}} < 75$.

4.3. The Wind–Luminosity Relation

Figure 12 plots the modified wind momentum (the product of the mass-loss rate times the terminal wind speed times the square root of the stellar radius; Kudritzki et al. 1995) versus stellar luminosity. Filled circles denote luminosity class V and IV objects while open circles are luminosity classes I–III. As in Figure 8, blue squares enclose objects that face an $8\ \mu\text{m}$ bright-rimmed cloud, while green circles enclose objects where the minimum peculiar velocity was assigned, and orange circles enclose objects that are candidate radiation bow waves, $L_*/L_{\text{IR}} < 75$. Because of the log scale, the uncertainties are similar for all data points. A single error bar denotes typical uncertainties which are dominated by the temperature

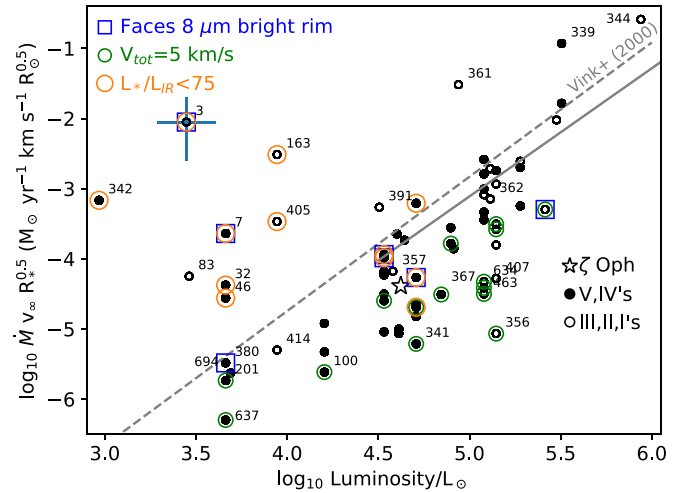


Figure 12. Modified wind momentum vs. stellar luminosity. The gray solid and dashed lines denote the theoretical relations for stars 27,500–50,000 K and 12,500–22,500 K, respectively (Vink et al. 2000). Filled circles denote luminosity class V and IV objects while open circles are luminosity classes I–III. Because of the log scale, the uncertainties are similar for all data points; a single error bar denotes typical uncertainties.

Table 4
Objects in Special Categories

Category	ID
$V_{\text{tot}} < 5\ \text{km s}^{-1}$	16, 100, 201, 320, 338, 341, 356, 367, 392, 463, 637
Faces $8\ \mu\text{m}$ bright-rimmed cloud	3, 7, 380, 384, 101, 555, 709
Bow wave candidate, $L_*/L_{\text{IR}} < 75$	3, 7, 32, 46, 67, 101, 129, 163, 289, 243, 405, 555, 626, 653, 709

Note. (1) Object classification denoting special object categories according to the criteria discussed in Section 4. (2) Identification numbers of objects in each category.

uncertainty of 10% (x axis) and the uncertainties on the mass-loss rates (Table 3) and terminal wind velocities (y axis). The gray solid and dashed lines are theoretical relations for stars 27,500–50,000 K and 12,500–22,500 K, respectively (Vink et al. 2000, Equations (15) and (17)), representing both sides of the nominal bistability jump.

The dispersion among the data points is large, but a correlation is clear, consistent in slope with the theoretical wind–luminosity relation. The data fall systematically below this theoretical relation by about 0.4 dex. Notably, the green circles fall exclusively on the low side of the trend and below model predictions. Most of the objects that lie above model predictions are candidate radiation bow waves, and these often coincide with nebulae that face an $8\ \mu\text{m}$ bright-rimmed cloud. The most deviant objects in Figure 8, #3, #163, #342, and #361, also lie furthest from the theoretical relation in this figure. Possible reasons for their departure from theoretical expectations have been discussed earlier. The cool (B5–B8II, but highly uncertain) objects #83 and #391 appear on this plot but not in previous figures, where they fall off the cool end of the axis range. Both lie considerably in excess of the predicted relation, but neither is identified as a probable radiation bow wave nebula. Both objects are cool enough that the second bistability jump near 10,000 K may be relevant. Object #361 (B2I) also lies well above the expected relation, but its

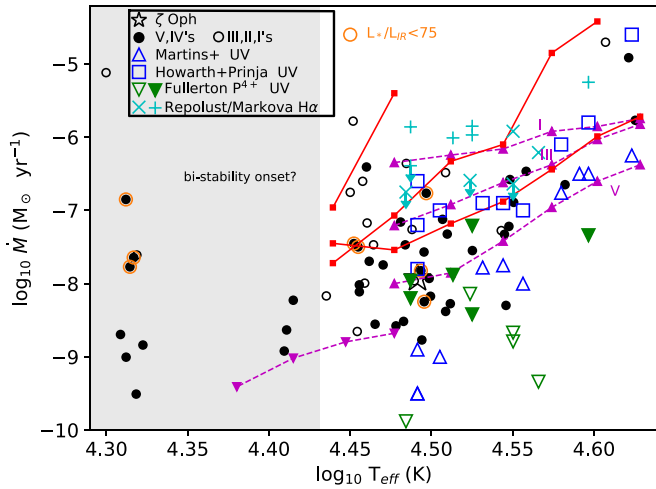


Figure 13. Mass-loss rate vs. effective temperature for dwarfs (filled circles) and evolved stars (open circles) from the bow shock sample. Open blue triangles and squares depict observational results from the sample of Galactic O3–O9 main-sequence stars as measured by Martins et al. (2005b) and Howarth & Prinja (1989), respectively. Green open and filled triangles depict the dwarfs and giants, respectively, measured using the ultraviolet P⁴⁺ line (Fullerton et al. 2006). Cyan ×’s and +’s depict the same stars as determined from the H α line (Markova et al. 2004; Repolust et al. 2004). Red and magenta lines mark theoretical predictions, as in previous figures.

temperature and luminosity is very poorly constrained by the available data. Once the candidate radiation bow wave nebulae are removed, the remaining data in Figure 12 show good agreement with the slope of the theoretical wind–luminosity relation, but with a zero-point offset of about 0.4 dex toward lower values.

4.4. Comparison with Prior Data

Figure 13 replicates Figure 8 and includes mass-loss rates measured for the set of Galactic O3–O9.5 dwarf stars from Martins et al. (2005b; blue open triangles) and Howarth & Prinja (1989; blue open squares), respectively.¹⁴ The Martins et al. (2005b) mass-loss rates derived from UV spectra fall somewhat below the bow shock sample, increasingly so in the regime of late O stars. The mass-loss rates given by Howarth & Prinja (1989) lie consistently above those in the present sample. The Howarth & Prinja (1989) values are broadly consistent with the Lucy (2010) theoretical expectations for dwarfs, but above the Krtićka & Kubát (2017) relation. Figure 13 also shows the late O dwarf and giant stars with mass-loss rates determined from ultraviolet P⁴⁺ absorption lines (Fullerton et al. 2006; green open and filled triangles, respectively) and the same set of stars determined from the H α line (Markova et al. 2004; Repolust et al. 2004; cyan +’s and ×’s). The P⁴⁺-based estimates show a large dispersion and lie consistently below the mean of the bow shock sample, but there is some overlap. The H α results (for homogeneous winds) lie far above the mean of the bow shock stars by factors of 10 or more. Some are upper limits, indicated by arrows, and are consistent with the bow shock estimates. This suggests that corrections for clumping in stellar winds are significant, factors of 3–10, consistent with inferences from other works (e.g., see the review by Puls et al. 2008). Unfortunately, there are no objects in common (with the exception of ζ Oph) between the

bow shock sample and the UV-based and H α -based studies, so direct comparisons must await future works. Overall, Figure 13 shows that the bow shock sample agrees reasonably well with UV-based estimates, but lacks examples of extremely low mass-loss rates $\dot{M} < 10^{-9} M_{\odot} \text{ yr}^{-1}$ that typify the weak-wind phenomenon. The bow shock sample also extends observational results into the regime of B0–B2 dwarfs that are not probed by other methods.

5. Discussion and Conclusions

Application of the physical requirement for momentum balance between a stellar wind and an impinging ISM yields a new method of mass-loss measurements for a sample of 67 early-type stars. The inferred relation between mass-loss rate, and stellar temperature and luminosity agrees well with several sets of theoretical models for main-sequence and evolved stars hotter than about 25,000 K, especially when models accounting for bistability behavior are employed, e.g., Figure 9. However, the mean mass-loss rates are lower by factors of about 2.7 compared to the canonical Vink et al. (2001) prescription, even allowing for a reduction of theoretical rates required by the adoption of lower solar metallicity. This factor of ≈ 2.7 is consistent with the proposed reductions of 2–3 discussed in the literature and inferred from other measurement methods (summarized by Puls et al. 2015). The derived mass-loss rates are in reasonable agreement with—but slightly larger than—the theoretical predictions of Krtićka & Kubát (2017). Our data represent the first mass-loss estimates for dwarf stars in the very late O and early B spectral ranges.

At temperatures cooler than 25,000 K the agreement is less good but is considerably better when bistability physics is applied rather than ignored, i.e., the black versus the red points in Figure 9. We interpret this better agreement as a soft empirical confirmation that the prescriptions of Vink et al. (2001) get the temperature range and magnitude of bistability effects approximately correct. Some of the cool objects in Figure 9 show excellent agreement with predictions while others show exceedingly high mass-loss rates compared to models. Some of these large deviations may be explained by additional effects, such as when stars facing an 8 μm bright-rimmed cloud experience an impinging photoevaporative flow which amplifies the nebular surface brightness. Five of the seven such objects in our sample (blue squares in Figures 9 and 12) show elevated mass-loss rates compared to predictions. The majority of the most discrepant data are also probable radiation-driven bow waves where the nebula is becoming optically thick to UV photons. In these cases, the inferred mass-loss rates can be regarded as upper limits. Such objects should be discarded from efforts to measure mass-loss rates unless corrections can be developed. In the few cases where the derived mass-loss rates lie below predictions, some of these objects face giant H II regions where bulk outflows may produce a greater star–ISM relative velocity than what we derive from *Gaia* proper motions, leading to an underestimate of \dot{M} . For some objects, *Gaia* proper motions imply an unrealistically low peculiar stellar velocity, given the distinct arcuate nebulae observed, so we have assigned a minimum V_{tot} of 5 km s^{−1}. Ten of 11 such stars show mass-loss rates below the mean of the sample, leading us to consider these estimates of the mass-loss rates to be lower limits. This sample, as a whole, exhibits the power-law relation between modified wind momentum and luminosity very similar in slope—but not in

¹⁴ We have shifted the effective temperatures assigned by Martins et al. (2005b) by −2000 K for consistency with the O9.5V objects in our sample.

zero point—to that predicted from classical wind momentum arguments (Figure 12). Outliers on this figure closely track the deviations observed in Figure 9. The coolest objects show the largest discrepancies, and most of these outliers appear to be examples of radiation dust waves than true wind bow shocks (Henney & Arthur 2019). Such objects will warrant careful investigation on a case-by-case basis.

While the mean mass-loss rates agree well with recent theoretical expectations of Krtićka & Kubát (2017) across much of the temperature range in the current sample, the dispersion is large, an indication of substantial sources of random error. The tabulated uncertainties on \dot{M} average 42%. This does not include systematic uncertainties on dust emission coefficients or contributions from errors on the peculiar velocity—a very significant source of error owing to the velocity-squared dependence. We expect this term to dominate the uncertainties and contribute greatly to the observed dispersion in the mass-loss rates, especially in light of the (unquantifiable) contributions from bulk flows in the ISM, with magnitudes 30 km s^{-1} or larger (Bodenheimer et al. 1979; Tenorio-Tagle 1979). All of the other terms in Equation (2) which contribute to the sources of random error are well constrained or contribute only linearly to \dot{M} . We may also be seeing true variation in \dot{M} at a given spectral type that results from second-order effects such as rotation velocity, metallicity, binarity, or stellar age.

These new results are noteworthy for being the first mass-loss measurements in a sizable sample of early B dwarf and giant stars. As a new physically independent technique for measuring mass-loss rates, our approach is thought to be unaffected by the same systematic effects (e.g., clumping, assumptions about dominant state of ionization) that have led to highly discrepant results from canonical techniques. However, there are new sources of systematic error to consider. Adoption of a slightly different calibration of stellar terminal wind speeds would lead to a systematic increase in wind speeds by a factor of 1.5 and a decrease in the derived mass-loss rates by the same factor. Working in the opposite direction is a systematic increase of the stars’ peculiar velocities; if we were to consider the full three-dimensional motions, the V_{tot} values could increase by as much as 22%, on average, which would raise the derived mass-loss rates by a factor of 1.49. There remains the possibility that bulk ISM flows generate larger star–ISM relative velocities than those measured from proper motions, potentially raising the derived mass-loss rates by significant factors for what we expect to be only a small subset of objects. Additional systematic uncertainties on the dust emission coefficients at the level of 60% need to be considered as well. Adoption of updated physically specified dust emission coefficients surrounding hot stars, when available, could further revise the derived mass-loss rates. On one hand, additional heating from wind shocks could elevate the dust emission coefficients beyond those used here, thereby reducing the derived mass-loss rates. Indeed, Kobulnicky et al. (2017) noted that the infrared dust color temperatures of bow shock nebulae exceeded those expected from reprocessing-of-stellar-photons arguments. On the other hand, shocks could also destroy grains, thereby reducing dust emission coefficients. We are unable to estimate the magnitude (or even the sign!) of a revision to the Draine & Li (2007) emission coefficients in bow shock nebula environments on the basis of existing work. This

issue remains, in our opinion, the largest source of systematic uncertainty on our approach to deriving mass-loss rates.

Ultimately, a larger sample of bow-shock-producing B1–B3 stars of all evolutionary phases needs to be studied to understand the characteristics of stars that are typical of this population. We expect an expanded sample will preferentially have small standoff distances and/or faint bow shock nebulae, and may not be plentiful in the present angular-resolution-limited samples. Knowledge of the rotation rates (at least for B dwarfs) and evolutionary status of bow-shock-producing B stars will also be important for a more complete understanding of these initial results. One intriguing idea raised by the apparent success of the present results is to use the principles of bow shock physics outlined here to measure the speed of bulk ISM flows. This would require that mass-loss rates are securely established through other observational or theoretical means. Then, Equation (2) could be solved for V_a and, once peculiar stellar motions are removed, the bulk ISM speeds could be measured. Stellar bow shocks could then truly become the “interstellar weather vanes” presaged by Povich et al. (2008). Future releases of the *Gaia* data will provide improved distances and proper motions, reducing uncertainties on this sample of stars while opening up a larger sample of bow shock stars to analysis. Additional spectroscopy covering the blue/ultraviolet portion of the optical spectrum could provide much-needed stellar temperatures and wind speeds for each object in the sample. While obtaining these data remains an objective of our group’s efforts, the faint magnitudes and high interstellar extinctions will necessitate substantial observational resources. Theoretical work on dust emission coefficients that includes the role of stellar-wind shocks as well as radiant heating would help place the present results on more secure foundation.

This work has been supported by the National Science Foundation through grants AST-1412845 and AST-1411851. We offer our abundant gratitude to the reviewer, Jo Puls, for several detailed readings and many expert suggestions that substantially improved this work. Curt Struck alerted us to the work of William Henney on radiation-driven bow shocks. Exchanges with William Henney contributed greatly to this manuscript and prevented an error in the selection of dust grain emission coefficients. We also thank Rico Ignace, Derek Massa, and Eigen Li for their input at various stages of completion.

Facilities: APO, WIRO, SST, HSO, *Gaia*.

Software: IRAF, Tody (1986), SpeXtool, Cushing et al. (2004).

Appendix

This appendix includes discussions of individual objects based on optical or infrared spectra obtained at the Apache Point Observatory in 2017 and 2018 and optical spectra reported in W. T. Chick et al. (2019, in preparation). For each object, we have matched the apparent central star to objects in the GDR2 catalog. For each star, we provide the *Gaia* identifier and the *Gaia* (*G*) magnitude. We have also estimated spectrophotometric distances using the 2MASS *K* magnitude, and we have adopted absolute magnitudes and colors from Pecaut & Mamajek (2013). We correct for interstellar extinction using the Rayleigh–Jeans color excess prescription of Majewski et al. (2011). Discrepancies between

spectrophotometric distances and parallax distances are used to refine the luminosity class of stars that typically cannot be determined from the spectra alone. Radial velocities measured from optical spectra are given in the heliocentric frame and are based on the He I 5875.75 Å centroid (in-air wavelength). Velocities from infrared spectra are based on the Br 12 line at 16411.55 Å and Br 13 line at 16113.60 Å (vacuum wavelengths), determined from PHOENIX model atmospheres (also given in the vacuum wavelengths) for hot stars (Husser et al. 2013). Velocity uncertainties are limited by the S/N of the spectra and the broad nature of spectral features in massive stars, but are estimated to be at 6–11 km s⁻¹ including systematic calibration uncertainties. Velocities, in most cases, result from a single optical or infrared spectral measurement; given the prevalence of binary systems with semi-amplitudes of hundreds of km s⁻¹ among massive populations, these velocities should be taken as indicative but not a definitive measure of the systemic radial velocity.

G000.1169–00.5703 (#1)—Our infrared spectrum of this star (GID = 4057291747277127040, $G = 10.7$ mag) shows strong Br γ emission and He I 2.1126 μ m in emission and He II 2.1885 in absorption with an EW of about 1 Å. The spectral features and photometric properties are consistent with an O8Ve star at the parallax distance of $D_{\text{par}} = 2441^{+450}_{-332}$ pc. $V_{\odot} = -15$ km s⁻¹.

G001.0563–00.1499 (#3)—Our optical spectrum of this $G = 16.3$ mag, 2MASS $H = 11.1$ mag star (GID = 4057634103373474560) observed at 2.1 airmasses is faint and shows H α but no He lines in our low-S/N optical spectrum. Our infrared spectrum shows weak He I. Its parallax distance (D_{par}) of 1527^{+242}_{-184} pc would be consistent with its spectrophotometric distance (D_{spec}) if it were a B5III, so we have adopted this classification. There are no other candidate stars at the geometric center of the arcuate nebula. The H α velocity is $V_{\odot} = -39$ km s⁻¹, which agrees roughly with the -15 km s⁻¹ measured from the H lines in our infrared spectrum, so we adopt -27 km s⁻¹. The large proper motion in decl. of -12 mas yr⁻¹ is much larger than any other star within 30'' and is consistent with the bow shock orientation, making this a strong candidate for the source of the bow shock nebula. The nebulae appears projected inside a larger broken ellipse of bright 8 μ m PAH emission and has PAH emission at the location of the 24 μ m arcuate nebula.

G003.8417–01.0440 (#7)—Strong He I lines are present in the optical and infrared spectra of this $G = 12.7$ mag object (GID = 4064254301560852352), but no He II are evident. B2V fits the spectrum well, but leads to a $D_{\text{spec}} = 2000$ pc—slightly larger than $D_{\text{par}} = 1313^{+89}_{-78}$ pc. The radial velocity computed from optical He lines is -0.5 km s⁻¹, in exact agreement with the radial velocity derived from the infrared H lines. The SST images shows additional nebulosities preceding the 24 μ m bow shock, suggesting an interaction with a more extended interstellar structure. No other *Gaia* sources are located within 10'', but there is a collection of other stellar sources 20'' to the southwest, so there may be other contributions to the ultraviolet flux that illuminates this region containing several arcuate objects.

G005.5941+00.7335 (#11)—B0V (GID = 4067804899497964416; $G = 13.9$ mag) fits the He and H lines in the optical spectrum well, predicting $D_{\text{spec}} = 2400$ pc versus $D_{\text{par}} = 2446^{+437}_{-325}$ pc. $V_{\odot} = +18.8$ km s⁻¹. Lines are especially narrow, suggesting the possibility of an evolved luminosity class, but

our optical spectrum is not of sufficient quality to discern. The positive decl. proper motion of 1.4 mas yr⁻¹ contrasts with other nearby objects, which are negative, and is consistent with the bow shock orientation.

G006.2812+23.5877 (#13)— ζ Oph (GID = 4337352305315545088, $G = 2.4$ mag) is the prototypical runaway bow shock star, an O9.2IV. We adopt the radial velocity of $V_{\odot} = -15$ km s⁻¹ and calculate its peculiar velocity from its *HIPPARCOS* parallax (distance of 112 pc), proper motion, and radial velocity rather than the *Gaia* data which carry larger uncertainties.

G006.8933+00.0743 (#16)—B0 provides a good match to the optical spectrum this star (GID = 4069437463777653632, $G = 11.7$ mag). $D_{\text{par}} = 3008^{+801}_{-534}$ is consistent with $D_{\text{spec}} = 2760$ pc only if the luminosity class is near III. $V_{\odot} = -24$ km s⁻¹.

G011.0709–00.5437 (#26)—A probable O9V (GID = 4094704481502396288, $G = 11.7$ mag) this star shows weak He II 5410 Å in our optical spectrum. It has $D_{\text{par}} = 3060^{+471}_{-364}$ pc, somewhat larger than $D_{\text{spec}} = 2280$ pc, but this discrepancy could be reconciled if it were an equal-luminosity binary. $V_{\odot} = -1$ km s⁻¹.

G011.6548+00.4943 (#28)—This star (GID = 4095751942430811776, $G = 13.2$ mag) is approximately a B0V from our optical and infrared spectra, which are poor in quality. $D_{\text{par}} = 2409^{+445}_{-329}$ pc agrees reasonably with $D_{\text{spec}} = 1980$ pc. $V_{\odot} = -27$ km s⁻¹ from our infrared spectrum.

G012.3407–00.3949 (#32)—From the strong H I lines and weak He I and absent He II in our infrared spectrum we classify this star (GID = 4095629759211238400, $G = 13.8$ mag) as early B. The He I features appear doubled, with components at -126 km s⁻¹ and 308 km s⁻¹, but the S/N is low and the velocities are considerably uncertain. Our optical spectrum on 2018 June 13 looks double-featured in the He I lines, with components at -133 and 257 km s⁻¹. The white-light guide camera images appear elongated east–west for this object, suggesting the possibility of a visual double with a sub-arcsecond separation. We adopt B2V+B2V which provides good agreement between $D_{\text{par}} = 2398^{+626}_{-419}$ pc and $D_{\text{spec}} = 2560$ pc. $V_{\odot} = 32$ km s⁻¹. We have arbitrarily divided the mass loss rates for this object by two as a correction for the double nature of the source.

G014.4703–00.6427 (#46)—(GID = 4097416946633635584, $G = 16.5$ mag) The EW of He I 2.1126 μ m is 1.01 Å making this a probable B2 star, likely a dwarf star given its parallax distance of $D_{\text{par}} = 688^{+163}_{-111}$ pc. With $H = 9.5$ mag and $G = 16.5$, the implied reddening is $A_K = 1.2$ mag ($\simeq A_V \simeq 11$ mag.), unusually large for such a small distance. $V_{\odot} = -32$ km s⁻¹, -17 km s⁻¹, and -4 km s⁻¹ on 2018 May 3, 2018 June 3, 24, respectively from our infrared spectra, so we adopt an average of -18 km s⁻¹.

G017.0826+00.9744 (#67)—An O9V based on classification by Evans et al. (2005; NGC 6611ESL45; GID = 4146617819936287488, $G = 11.5$ mag) $D_{\text{par}} = 1507^{+123}_{-106}$ pc. Our optical spectrum shows from 2018 June 13 yields $V_{\odot} = +9$ km s⁻¹ and displays He II 5410 with a EW of about 0.6 Å, consistent with this classification and suggests $D_{\text{spec}} = 2010$ pc. This target appears to be a visual double with a separation of about $1''.5$, position angle $PA \simeq 50^\circ$, and a flux difference of at least five magnitudes and the brighter component to the northeast.

G019.8107+00.0965 (#83)—(GID = 41533761786229465 60, $G = 14.3$ mag) Our optical spectrum shows broad and very weak He I lines, suggesting a mid-late B star. A velocity measured from the broad (16 Å FWHM) H α line yields $V_{\odot} \simeq 0$ km s $^{-1}$. $D_{\text{par}} = 2709^{+318}_{-259}$ pc is consistent with a B2II at $D_{\text{spec}} = 3210$ pc. The luminosity class is very uncertain.

G023.0958+00.4411 (#100)—The optical spectrum of this star (GID = 4156581976571298944, $G = 13.4$ mag) is of poor quality, but the strength of He I in a B2V yields good agreement with the spectrum and between $D_{\text{par}} = 1819^{+247}_{-195}$ pc and $D_{\text{spec}} = 1910$ pc. $V_{\odot} = +15$ km s $^{-1}$.

G023.1100+00.5458 (#101)—B0V provides a good fit to the optical spectrum of this star (GID = 4156594925877520512, $G = 12.1$ mag). $D_{\text{par}} = 2330^{+460}_{-333}$ pc agrees well with $D_{\text{spec}} = 2043$ pc. $V_{\odot} = +14$ km s $^{-1}$.

G027.3338+00.1784 (#129)—With a parallax distance of $D_{\text{par}} = 870^{+79}_{-66}$ pc this star (GID = 4256681923166288640, $G = 10.1$ mag) displays the CO bandhead features redward of 2.4 μ m, characteristic of cool stars. M0III provides a reasonable fit to the optical spectral properties for a spectroscopic distance of $D_{\text{spec}} = 930$ pc. Cross correlating the K -band spectrum with a PHOENIX model atmosphere for $T = 4000$ K, $\log(g) = 2.0$, and solar metallicity results in a velocity of $V_{\odot} = -25$ km s $^{-1}$. This is one of only three stars in the present sample that is not a hot, early-type star, although it may be a descendant of a massive star. The central star of the nebula is bright and unambiguous, and there are no other *Gaia* sources within 6".

G031.9308+00.2676 (#163)—We estimate this star (GID = 4266110686393370112, $G = 13.2$ mag) as B3Ile owing to the weak H α compared to the He I lines in our optical spectrum. The evolved luminosity class provides $D_{\text{spec}} = 5760$ pc, a somewhat questionable match to $D_{\text{par}} = 4438^{+849}_{-629}$ pc. This object exhibits a considerable redshift at $V_{\odot} = +71$ km s $^{-1}$.

G037.2933+00.6703 (#201)—Our infrared spectrum of this star (GID = 4281150081268339072, $G = 16.3$ mag) shows He I 2.1126 μ m in absorption. The parallax distance of $D_{\text{par}} = 1088^{+324}_{-205}$ pc agrees well with the spectrophotometric distance of $D_{\text{spec}} = 1105$ pc for a B2V. Our optical spectrum of a slightly brighter $G = 15.1$ star, GID = 4281150081268339456, which lies about 3" to the west-southwest, is similar to a K3III, consistent with the parallax distance of 630 pc for that star.

G055.5792+00.6749 (#289)—Our two infrared spectra of this star (GID = 2017772886883963392, $G = 12.3$ mag) from 2018 May 29 and 2018 June 3 show strong CO bandhead features near 2.4 μ m. $V_{\odot} = 15$ km s $^{-1}$ and $V_{\odot} = 21$ km s $^{-1}$ on the two nights, respectively, by cross correlation with an M0III which provides a reasonable match to the spectral features and to the photometric properties ($D_{\text{spec}} = 2150$ pc and $D_{\text{par}} = 2138^{+256}_{-208}$ pc). We adopt $V_{\odot} = 18$ km s $^{-1}$. The field contains multiple 24 and 70 μ m arcs and prominent stars, creating considerable ambiguity about the geometry and nature of this object (Kobulnicky et al. 2016, Figure 13.289).

G073.6200+01.8522 (#320)—W. T. Chick et al. (2019, in preparation) gives B0III (HD 191611; GID = 205923619625-0413696, $G = 8.5$ mag) but O9III provides a better match between $D_{\text{par}} = 2509^{+254}_{-212}$ pc and $D_{\text{spec}} = 2450$ pc. $V_{\odot} = 3$ km s $^{-1}$ (W. T. Chick et al. 2019, in preparation).

G074.3117+01.0041 (#322)—W. T. Chick et al. (2019, in preparation) classifies this star (GID = 2060507437839909248, $G = 12.6$ mag) as O8V, albeit with some uncertainty. With

$D_{\text{par}} = 4460^{+605}_{-481}$ pc, consistency with $D_{\text{spec}} = 4462$ pc is achieved by assigning O8IV, consistent with its spectrum. $V_{\odot} = -15$ km s $^{-1}$ (W. T. Chick et al. 2019, in preparation). This object appears to lie inside of, but does not directly face an 8 μ m bright-rimmed cloud.

G077.0505-00.6094 (#329)—As an O8V (KGK 2010-10; GID = 2063868163830050176, $G = 14.1$ mag) $D_{\text{spec}} = 2710$ pc, slightly larger than the parallax distance $D_{\text{par}} = 2115^{+280}_{-223}$ pc. $V_{\odot} = -39$ km s $^{-1}$ (W. T. Chick et al. 2019, in preparation). A contribution from a hypothetical companion would easily resolve this discrepancy.

G078.2869+00.7780 (#331)—Vijapurkar & Drilling (1993) lists this star (LSII+39 53; GID = 2067267299727875584, $G = 9.9$ mag) as O7V which yields $D_{\text{spec}} = 1760$ pc, consistent with $D_{\text{par}} = 1594^{+116}_{-101}$ pc. $V_{\odot} = -51$ km s $^{-1}$ (W. T. Chick et al. 2019, in preparation).

G078.5197+01.0652 (#333)—Our optical spectrum for this object (GID = 2067382031192434816, $G = 13.0$ mag) from 2018 June 13 shows doubled He I features with approximately equal depth at -241 and $+205$ km s $^{-1}$. There is no indication of He II. It has $D_{\text{par}} = 1554^{+245}_{-188}$ pc, consistent with $D_{\text{spec}} = 1410$ pc for two B0V's.

G079.8223+00.0959 (#338)—This probable O8V (CPR 2002A10; GID = 2064738049323468928, $G = 13.8$ mag) has $D_{\text{par}} = 1792^{+225}_{-181}$ pc, consistent with $D_{\text{spec}} = 1600$ pc and $V_{\odot} = -10$ km s $^{-1}$ (W. T. Chick et al. 2019, in preparation).

G080.2400+00.1354 (#339)—This O5V (CPR 2002A37; GID = 2064838375463800448, $G = 11.7$ mag) has $D_{\text{par}} = 1703^{+129}_{-112}$ pc, consistent with $D_{\text{spec}} = 1590$ pc. $V_{\odot} = -43$ km s $^{-1}$ (W. T. Chick et al. 2019, in preparation).

G080.8621+00.9749 (#341)—Classified as O9V by W. T. Chick et al. (2019, in preparation) this star (KGK 2010-1; GID = 2067963015711183744, $G = 12.1$ mag) has $D_{\text{par}} = 1622^{+82}_{-73}$ pc, consistent with $D_{\text{spec}} = 1590$ pc. $V_{\odot} = -38$ km s $^{-1}$ (W. T. Chick et al. 2019, in preparation).

G080.9020+00.9828 (#342)—This mid-B star (KGK 2010-2; GID = 2067963535403817728, $G = 14.5$ mag) displays weak He I in our optical and infrared spectra, but strong H I features. B4V fits the spectral features and provides consistency with between the parallax distance of $D_{\text{par}} = 1538^{+82}_{-73}$ pc and the $D_{\text{spec}} = 1720$ pc. Our infrared spectrum of this star on 2018 June 3 indicates $V_{\odot} = -17$ km s $^{-1}$ which compares favorably to the average value of optical spectra from W. T. Chick et al. (2019, in preparation), $V_{\odot} = -7$ km s $^{-1}$.

G082.4100+02.3254 (#344)—This well-studied O4If (BD +43 3654; GID = 2069819545390584192, $G = 9.1$ mag) has $D_{\text{par}} = 1577^{+81}_{-74}$ pc, consistent with $D_{\text{spec}} = 1460$ pc. W. T. Chick et al. (2019, in preparation) reports $V_{\odot} = -36$ km s $^{-1}$.

G104.3447+02.2299 (#353)—A strong He II 5410 Å makes this star (GID = 2201205412482296448, $G = 11.6$ mag) a probable O5V, yielding consistency between $D_{\text{par}} = 3932^{+468}_{-380}$ pc and $D_{\text{spec}} = 4370$ pc. $V_{\odot} = -47$ km s $^{-1}$ from W. T. Chick et al. (2019, in preparation). H α appears in emission and possibly variable.

G106.6327+00.3917 (#356)—An early B temperature class (HD 240015; GID = 2008430237808841600, $G = 9.8$ mag), the parallax distance of $D_{\text{par}} = 2583^{+226}_{-193}$ pc requires about B0III for consistency at $D_{\text{spec}} = 2690$ pc. $V_{\odot} = -54$ km s $^{-1}$ (W. T. Chick et al. 2019, in preparation).

G106.6375+00.3783 (#357)—(HD 240016; GID = 200838-3302396655488; $G = 9.4$ mag) $D_{\text{par}} = 1493^{+72}_{-65}$ pc is consistent

with $D_{\text{spec}} = 1410$ pc for a B2III. $V_{\odot} = -88$ km s $^{-1}$ W. T. Chick et al. (2019, in preparation).

G108.9891+01.5606 (#361)—A probable B1I, this star (TYC 4278-522-1; GID = 2206818556775783552, $G = 10.1$ mag) displays H α in emission and has $D_{\text{par}} = 3896^{+515}_{-412}$ pc, roughly consistent with $D_{\text{spec}} = 4870$ pc given the large uncertainties inherent in assigning magnitudes to supergiants. $V_{\odot} = -53$ km s $^{-1}$ (W. T. Chick et al. 2019, in preparation).

G109.1157+00.6799 (#362)—This very distant ($D_{\text{par}} = 5295^{+944}_{-714}$ pc) object (GID = 2014562519088745344, $G = 12.7$ mag) is a probable B2I or similar. $V_{\odot} = -33$ km s $^{-1}$ W. T. Chick et al. (2019, in preparation).

G133.1567+00.0432 (#367)—Strong He II matches an O7V at $D_{\text{spec}} = 2050$ pc for this star (LSI+60 226; GID = 507686819685070208, $G = 10.4$ mag) consistent with $D_{\text{par}} = 2131^{+130}_{-116}$ pc. Our two infrared spectra on 2017 July 13 and September 1 yield $V_{\odot} = -61$ km s $^{-1}$ and $V_{\odot} = 46$ km s $^{-1}$, suggesting that this is a single-lined spectroscopic binary.

G134.3552+00.8182 (#368)—Classified as O9.5V by Massey et al. (1995), this eruptive variable star (KM Cas; GID = 465523778576137600, $G = 10.8$ mag) appears somewhat hotter in our 2018 June 13 optical spectrum, perhaps O8.5V. H α is very weak, suggesting emission has filled some H I features. It has $D_{\text{par}} = 2298^{+187}_{-161}$ pc, somewhat larger than the spectrophotometric distance of $D_{\text{spec}} = 1690$ pc for an O9.5V but consistent with the $D_{\text{spec}} = 2040$ pc for an O8.5V, or it may be slightly evolved and more luminous as an O8.5IV. $V_{\odot} = -1$ km s $^{-1}$ from our infrared and optical spectra. There are additional absorption features present across the spectrum that are inconsistent with models of hot stars and may indicate circumstellar material.

G137.4203+01.2792 (#369)—Conti & Leep (1974) list this star (BD+60 586; GID = 464697873547937664, $G = 8.4$ mag) as O8III, which leads to $D_{\text{spec}} = 2790$ pc, in better agreement with the $D_{\text{par}} = 2762^{+427}_{-329}$ pc than the O7.5V given by Hillwig et al. (2006). O8III provides an excellent match to our optical spectrum of 2018 June 13. We adopt $V_{\odot} = -40$ km s $^{-1}$ from our optical spectrum, consistent with the $V_{\odot} = -49$ km s $^{-1}$ from the literature.

G223.7092-01.9008 (#380)—We adopt the B0IVe (HD 53367; GID = 3046530911350220416, $G = 7.0$ mag) given by Tjin A Djie et al. (2001), which predicts $D_{\text{spec}} = 369$ pc, which is considerably greater than $D_{\text{par}} = 129^{+12}_{-14}$ pc; however, *Gaia* parallaxes for very bright stars are especially uncertain as of this writing. We also adopt $V_{\odot} = 21$ km s $^{-1}$ from the literature. A B1V would be required in order to reconcile the parallax and spectrophotometric distances, so we provisionally adopt this classification.

G224.1685-00.7784 (#381)—We adopt the O7Vz given by Sota et al. (2014) for this star (HD 54662; GID = 3046582725837564800, $G = 6.1$ mag). This yields $D_{\text{spec}} = 985$ pc, in good agreement with $D_{\text{par}} = 1142^{+120}_{-100}$ pc. We also adopt $V_{\odot} = 57$ km s $^{-1}$ from the literature. The possible double-lined nature (O6.5V+O7V-O9V, 2119 day period) of this source reported by Boyajian et al. (2007) was not confirmed by Sota et al. (2014).

G224.7096-01.7938 (#382)—The parallax and proper motion for this B0III (Tjin A Djie et al. 2001) star (FN CMa; GID = 3046209987096803584, $G = 5.3$ mag) comes from the *HIPPARCOS* mission. The parallax distance of $D_{\text{par}} = 934$ pc

agrees well with the spectrophotometric distance of 637 pc. We adopt $V_{\odot} = 31$ km s $^{-1}$ from the literature.

G253.7104-00.1920 (#384)—We adopt O7III_{nn} from Vijapurkar & Drilling (1993) for this star (CD-35 4415; GID = 5543183649492723584, $G = 10.3$ mag) $D_{\text{par}} = 3791^{+463}_{-375}$ pc, consistent with $D_{\text{spec}} = 3580$ pc.

G268.9550-01.9022 (#391)—We adopt B7Iab from Houk (1978) for this Algol-type eclipsing binary (HD 77207; GID = 5325452481440825600, $G = 9.2$ mag). $D_{\text{par}} = 1851^{+106}_{-95}$ pc, which is vastly smaller than $D_{\text{spec}} = 6900$ pc. A few such large discrepancies are not surprising given the inherent difficulty in assigning luminosities to supergiants.

G269.2089-00.9138 (#392)—Listed generically in the literature as an OB star (CPD-47 3051; GID = 5326951150144920064, $G = 10.8$ mag), the parallax distance of $D_{\text{par}} = 1901^{+121}_{-136}$ pc and photometric data are consistent with a B0V ($D_{\text{spec}} = 2200$ pc).

G272.5794-01.7247 (#394)—We adopt B0 from Reed (2003) for this object (HD 298310; GID = 5313479796251809664, $G = 9.8$ mag). A B0III provides $D_{\text{spec}} = 2010$ pc, consistent with $D_{\text{par}} = 2199^{+155}_{-136}$ pc.

G273.1192-01.9620 (#395)—Reed (2003) lists this (HD 298353; GID = 5311906841793959936, $G = 9.8$ mag) as an O star. We adopt O7V, which provides $D_{\text{spec}} = 2450$ pc, consistent with $D_{\text{par}} = 2685^{+296}_{-244}$ pc.

G282.1647-00.0256 (#397)—For this star (CD-55 3196; GID = 5259053730157539328, $G = 10.5$) we adopt O9.5III (Parthasarathy et al. 2012), which produces good agreement between $D_{\text{par}} = 2513^{+186}_{-163}$ pc and $D_{\text{spec}} = 2320$ pc.

G286.0588-01.6633 (#404)—This star (CD-59 3123; GID = 5255179905867530752, $G = 9.1$ mag) is listed as O9.5Ib in Vijapurkar & Drilling (1993). With a parallax distance of $D_{\text{par}} = 3969^{+470}_{-545}$ pc, its photometric data would be consistent with the spectral type and luminosity class, $D_{\text{spec}} = 3601$ pc. The stellar driver of this bow shock was incorrectly identified as TYC 8613-707-1 in Kobulnicky et al. (2016, Figure 13.404; the brighter source to the upper right of TYC 8613-707-1 at the center is CD-59 3123) and Kobulnicky et al. (2017). The position and identification are corrected in this work.

G286.4644-00.3478 (#405)—Listed as B5 in Nesterov et al. (1995), this star (HD 303197; GID = 5350640192585837568, $G = 9.1$ mag) has $D_{\text{par}} = 2328^{+154}_{-136}$ pc, consistent with a B3III at that distance ($D_{\text{spec}} = 2270$ pc) but inconsistent with any early B dwarf.

G287.1148-01.0236 (#406)—HD 92607 (GID = 525447-8593582508288, $G = 8.1$ mag) is an O9Vn (Sota et al. 2014), predicting $D_{\text{spec}} = 2310$ pc, broadly consistent with $D_{\text{par}} = 2786^{+597}_{-424}$ pc.

G287.4071-00.3593 (#407)—HD 93249 (GID = 5350-395383778733568, $G = 8.3$ mag), an O9III+O binary (Sota et al. 2014), has $D_{\text{par}} = 3096^{+376}_{-304}$ pc, consistent with the expected $D_{\text{spec}} = 2880$ pc.

G287.6131-01.1302 (#409)—HD 93027 (GID = 52542-68518156437888, $G = 8.7$ mag), an O9.5IV (Sota et al. 2011) has $D_{\text{spec}} = 2940$ pc, similar to the $D_{\text{par}} = 3426^{+507}_{-395}$ pc. This is a single-lined eclipsing binary according to Sota et al. (2011), suggesting a significant difference in mass between the primary and secondary stars.

G287.6736-01.0093 (#410)—HD 305536 (GID = 52542-69961265754368, $G = 9.0$ mag) is an O9.5V+unknown binary candidate (Levato et al. 1990; Sota et al. 2014). $D_{\text{par}} = 2266^{+152}_{-134}$ pc is consistent with $D_{\text{spec}} = 2120$ pc.

G288.1505–00.5059 (#411)—HD 305599 (GID = 5338310–887667141888, $G = 9.9$ mag) is listed as O9.5V (Alexander et al. 2016). $D_{\text{par}} = 2071^{+145}_{-127}$ pc agrees roughly with $D_{\text{spec}} = 2500$ pc.

G288.3138–01.3085 (#413)—HD 93683 (GID = 524–2187050013731200, $G = 7.8$ mag) is given as an O9V + B0V binary (Alexander et al. 2016). $D_{\text{par}} = 1629^{+248}_{-191}$ pc is somewhat larger than $D_{\text{spec}} = 1090$ pc, even accounting for the possible binary, raising the possibility that one or both components may be slightly evolved. O9IV+B0IV would provide a closer match to the parallax distance and the observed mass-loss rate.

G288.4263–01.2245 (#414)—HD 93858 (GID = 52421–84954087251456, $G = 9.0$ mag) is an eclipsing binary with a B3II/III primary (Houk 1978). $D_{\text{par}} = 2602^{+196}_{-191}$ pc, broadly consistent with this luminosity class.

G308.0406+00.2473 (#463)—TYC 8995-1548-1 (GID = 5865357598905884288, $G = 11.6$ mag) is listed as an OB star (Stephenson & Sanduleak 1971) and B0III provides a good match to $D_{\text{par}} = 3689^{+618}_{-470}$ pc.

G326.7256+00.7742 (#555)—ALS 18049 (GID = 588–5668499206748160, $G = 12.2$ mag) is listed in the literature as O7V, but O9V provides a better match between $D_{\text{spec}} = 3120$ pc and $D_{\text{par}} = 2677^{+421}_{-323}$ pc.

G332.4863+00.8256 (#589)—CD-49 10393 (GID = 5935–169268617561344, $G = 11.1$ mag) is listed as an OB star (Stephenson & Sanduleak 1971). B0V provides good agreement with $D_{\text{par}} = 2533^{+306}_{-348}$ pc.

G340.4772–00.1528 (#624)—This star's (GID = 5964–264231754517504, $G = 13.3$ mag) infrared spectrum displays Br γ in emission but He I 2.1126 μm in absorption and no He II, making it a probable B emission-line star. $D_{\text{par}} = 3508^{+675}_{-496}$ pc, which requires something close to a B0IIIe for a consistent spectrophotometric distance. $V_{\odot} = +10$ km s $^{-1}$.

G340.8579–00.8793 (#626)—This object (GID = 5964–030074446095744, $G = 11.3$ mag) displays the Bracket series in absorption, He I 2.1126 μm in absorption, and weak He II 2.1885 μm , suggesting a late O star. $D_{\text{par}} = 2169^{+389}_{-288}$ pc, which is close to an O9V at $D_{\text{spec}} = 2290$ pc. $V_{\odot} = -13$ km s $^{-1}$.

G342.3422–00.4456 (#634)—(HD 152756; GID = 5964–575672745370752, $G = 8.8$ mag) shows strong He I and Bracket series absorption but no He II is present in the K -band spectrum. $D_{\text{par}} = 1802^{+220}_{-178}$ pc, which is an excellent match to a B0III at $D_{\text{spec}} = 1800$ pc. $V_{\odot} = -11$ km s $^{-1}$.

G342.5873+00.1600 (#635)—A probable late O star (GID = 5964883879575434240, $G = 13.5$ mag) showing He II with an EW of 1.2 Å, an O6V provides a good match to the parallax distance of $D_{\text{par}} = 2809^{+829}_{-544}$ pc and to the spectrum. $V_{\odot} = -26$ km s $^{-1}$.

G342.7172–00.4361 (#637)—Displaying He I lines, this star (GID = 5964678060440055296, $G = 15.2$ mag) is nearby at $D_{\text{par}} = 1315^{+193}_{-150}$ pc. The infrared spectrum and distance agrees well with a B2V at $D_{\text{spec}} = 1260$ pc. $V_{\odot} = -38$ km s $^{-1}$.

G344.4658–00.5580 (#648)—(GID = 5965562308305643008; $G = 14.3$ mag) This star shows H α in emission with no detectable helium lines, making the spectral type particularly uncertain. We estimate it near B0III, primarily on the basis of $D_{\text{spec}} = 1877$ pc agreeing with $D_{\text{par}} = 1893^{+597}_{-373}$ pc.

G346.1388–00.2184 (#653)—This target (GID = 59661–32787371809536; $G = 13.7$; $H = 10.2$ mag) has weak narrow

H α and weak features near 4383/85 Å in our optical spectrum that are probable iron lines. The spectral features suggest that this is a late G or early K spectral type, making it unlikely to be the star driving a bow shock nebula at $D_{\text{par}} = 1664^{+114}_{-100}$ pc. Such a distance would require a giant (K0III:) luminosity class for consistency with the optical and IR magnitudes. Five other *Gaia* sources within 8'' are 3–7 mag fainter. There is no other bright early-type candidate driving a star along the symmetry axis. The $G = 19.4$ ($H = 13.8$) star GID = 596613278735–8462848 is a candidate central star located 6'' to the N-NE. Given the lack of an identifiable early type driving star of an appropriate magnitude at this distance, the nature of this arcuate nebula is uncertain.

G346.2958+00.0744 (#655)—This probable B1V star (GID = 5966890930670155520; $G = 13.7$ mag) has $D_{\text{spec}} = 2650$ pc, consistent with the $D_{\text{par}} = 2168^{+251}_{-204}$ pc. The He I lines in our optical spectrum appear asymmetric, so this may be a double-lined binary with blended components. It has $V_{\odot} = -69$ km s $^{-1}$.

G349.5431–00.5952 (#673)—This B1V (GID = 5972–791773374952192; $G = 13.5$ mag) has $D_{\text{spec}} = 2900$ pc, in excellent agreement with $D_{\text{par}} = 2705^{+337}_{-272}$ pc. $V_{\odot} = -22$ km s $^{-1}$ from the average of our optical and infrared radial velocities.

G353.4162+00.4482 (#692)—Our optical spectrum of this star (GID = 5975945894262363776; $G = 10.7$ mag) is well fit by an O7V, in good agreement with Gvaramadze et al. (2011; O7.5V). $D_{\text{spec}} = 1810$ pc consistent with $D_{\text{par}} = 1717^{+171}_{-142}$. The He lines are slightly asymmetric, suggesting a possible blended binary. $V_{\odot} = -30$ km s $^{-1}$ assuming a single line profile.

G355.4972–00.7571 (#694)—(GID = 4053776191953892224; $G = 12.1$ mag) B2V matches the narrow He lines and hint of Mg II 4481 Å in our optical spectrum. $D_{\text{spec}} = 1570$ pc, consistent with $D_{\text{par}} = 1329^{+233}_{-173}$ pc. $V_{\odot} = -11.2$ km s $^{-1}$.

G356.6602+00.9209 (#700)—This B0V (GID = 405529–7370601329024; $G = 13.1$ mag) from our optical spectrum has $D_{\text{spec}} = 3200$ in good agreement with $D_{\text{par}} = 3370^{+664}_{-481}$ pc. $V_{\odot} = -25.2$ km s $^{-1}$.

G359.9536–00.5088 (#709)—This source (GID = 4057–277728502494080; $G = 11.4$ mag) displays doubled He I 5876 Å lines in our optical spectrum in a ratio of about 2:3 at $V_{\odot} = -133$ and 115 km s $^{-1}$, respectively. $D_{\text{spec}} = 2860$ for a B0V, in reasonable agreement with $D_{\text{par}} = 3091^{+539}_{-403}$ pc, given the probable binary nature.

ORCID iDs

Henry A. Kobulnicky  <https://orcid.org/0000-0002-4475-4176>

Matthew S. Povich  <https://orcid.org/0000-0001-9062-3583>

References

- Acreman, D. M., Stevens, I. R., & Harries, T. J. 2016, *MNRAS*, **456**, 136
- Alexander, M. J., Hanes, R. J., Povich, M. S., & McSwain, M. V. 2016, *AJ*, **152**, 190
- Anders, E., & Grevesse, N. 1989, *GeCoA*, **53**, 197
- Asplund, M., Grevesse, N., & Sauval, A. J. 2005, in ASP Conf. Ser. 336, Cosmic Abundances as Records of Stellar Evolution and Nucleosynthesis, ed. T. G. Barnes, III & F. N. Bash (San Francisco, CA: ASP), 25
- Bailer-Jones, C. A. L. 2015, *PASP*, **127**, 994
- Bailer-Jones, C. A. L., Rybizki, J., Fouesneau, M., Mantelet, G., & Andrae, R. 2018, *AJ*, **156**, 58

- Blaauw, A. 1961, *BAN*, **15**, 265
- Bodenheimer, P., Tenorio-Tagle, G., & Yorke, H. W. 1979, *ApJ*, **233**, 85
- Boyajian, T. S., Gies, D. R., Dunn, J. P., et al. 2007, *ApJ*, **664**, 1121
- Castelli, F., & Kurucz, R. L. 2003, in *IAU Symp. 210, Modelling of Stellar Atmospheres, Poster Contributions*, ed. N. Piskunov, W. W. Weiss, & D. F. Gray (Cambridge: Cambridge Univ. Press), A20
- Cohen, D. H., Wollman, E. E., Leutenegger, M. A., et al. 2014, *MNRAS*, **439**, 908
- Comeron, F., & Kaper, L. 1998, *A&A*, **338**, 273
- Conti, P. S., & Leep, E. M. 1974, *ApJ*, **193**, 113
- Crowther, P. A., Lennon, D. J., & Walborn, N. R. 2006, *A&A*, **446**, 279
- Cushing, M. C., Vacca, W. D., & Rayner, J. T. 2004, *PASP*, **116**, 362
- Draine, B. T. (ed.) 2011, *Physics of the Interstellar and Intergalactic Medium* (Princeton, NJ: Princeton Univ. Press)
- Draine, B. T., & Li, A. 2007, *ApJ*, **657**, 810
- Evans, C. J., Smartt, S. J., Lee, J.-K., et al. 2005, *A&A*, **437**, 467
- Ferland, G. J., Chatzikos, M., Guzmán, F., et al. 2017, *RMxAA*, **53**, 385
- Fullerton, A. W., Gies, D. R., & Bolton, C. T. 1996, *ApJS*, **103**, 475
- Fullerton, A. W., Massa, D. L., & Prinja, R. K. 2006, *ApJ*, **637**, 1025
- Gaia Collaboration, Brown, A. G. A., Vallenari, A., et al. 2018, arXiv:1804.09365
- Garmany, C. D., Olson, G. L., van Steenberg, M. E., & Conti, P. S. 1981, *ApJ*, **250**, 660
- Gies, D. R., & Bolton, C. T. 1986, *ApJS*, **61**, 419
- Gull, T. R., & Sofia, S. 1979, *ApJ*, **230**, 782
- Gvaramadze, V. V., Kniazev, A. Y., Kroupa, P., & Oh, S. 2011, *A&A*, **535**, A29
- Hanson, M. M., Conti, P. S., & Rieke, M. J. 1996, *ApJS*, **107**, 281
- Henney, W. J., & Arthur, S. J. 2019, *MNRAS*, **486**, 3423
- Hillwig, T. C., Gies, D. R., Bagnuolo, W. G., Jr., et al. 2006, *ApJ*, **639**, 1069
- Houk, N. 1978, *Michigan Catalogue of Two-dimensional Spectral Types for the HD Stars* (Ann Arbor, MI: Univ. Michigan)
- Howarth, I. D., & Prinja, R. K. 1989, *ApJS*, **69**, 527
- Husser, T.-O., Wende-von Berg, S., Dreizler, S., et al. 2013, *A&A*, **553**, A6
- Irgang, A., Wilcox, B., Tucker, E., & Schiefelbein, L. 2013, *A&A*, **549**, A137
- Johnson, D. R. H., & Soderblom, D. R. 1987, *AJ*, **93**, 864
- Kiminki, D. C., Kobulnicky, H. A., Vargas Álvarez, C. A., Alexander, M. J., & Lundquist, M. J. 2015, *ApJ*, **811**, 85
- Kobulnicky, H. A., Chick, W. T., & Povich, M. A. 2018, *ApJ*, **856**, 74
- Kobulnicky, H. A., Chick, W. T., Schurhammer, D. P., et al. 2016, *ApJS*, **227**, 18
- Kobulnicky, H. A., & Fryer, C. L. 2007, *ApJ*, **670**, 747
- Kobulnicky, H. A., Gilbert, I. J., & Kiminki, D. C. 2010, *ApJ*, **710**, 549
- Kobulnicky, H. A., Kiminki, D. C., Lundquist, M. J., et al. 2014, *ApJS*, **213**, 34
- Kobulnicky, H. A., Schurhammer, D. P., Baldwin, D. J., et al. 2017, *AJ*, **154**, 201
- Krtićka, J. 2014, *A&A*, **564**, A70
- Krtićka, J., & Kubát, J. 2007, *A&A*, **464**, L17
- Krtićka, J., & Kubát, J. 2017, *A&A*, **606**, A31
- Kudritzki, R.-P., Lennon, D. J., & Puls, J. 1995, in *Science with the VLT*, ed. J. R. Walsh & I. J. Danziger (Berlin: Springer), 246
- Kudritzki, R.-P., & Puls, J. 2000, *ARA&A*, **38**, 613
- Lamers, H. J. G. L. M., Snow, T. P., & Lindholm, D. M. 1995, *ApJ*, **455**, 269
- Langer, N. 1998, *A&A*, **329**, 551
- Lanz, T., & Hubeny, I. 2003, *ApJS*, **146**, 417
- Leitherer, C. 1988, *ApJ*, **326**, 356
- Levato, H., Malaroda, S., Garcia, B., Morrell, N., & Solivella, G. 1990, *ApJS*, **72**, 323
- Lucy, L. B. 2010, *A&A*, **524**, A41
- Majewski, S. R., Zasowski, G., & Nidever, D. L. 2011, *ApJ*, **739**, 25
- Marcolino, W. L. F., Bouret, J.-C., Martins, F., et al. 2009, *A&A*, **498**, 837
- Markova, N., & Puls, J. 2008, *A&A*, **478**, 823
- Markova, N., Puls, J., Repolust, T., & Markov, H. 2004, *A&A*, **413**, 693
- Martins, F., Schaerer, D., & Hillier, D. J. 2005a, *A&A*, **436**, 1049
- Martins, F., Schaerer, D., Hillier, D. J., et al. 2005b, *A&A*, **441**, 735
- Massa, D., Fullerton, A. W., & Prinja, R. K. 2017, *MNRAS*, **470**, 3765
- Massey, P., Johnson, K. E., & Degioia-Eastwood, K. 1995, *ApJ*, **454**, 151
- Mathis, J. S., Mezger, P. G., & Panagia, N. 1983, *A&A*, **128**, 212
- Meyer, D. M.-A., Mignone, A., Kuiper, R., Raga, A. C., & Kley, W. 2017, *MNRAS*, **464**, 3229
- Meyer, D. M.-A., van Marle, A.-J., Kuiper, R., & Kley, W. 2016, *MNRAS*, **459**, 1146
- Mokiem, M. R., de Koter, A., Vink, J. S., et al. 2007, *A&A*, **473**, 603
- Muijres, L. E., Vink, J. S., de Koter, A., Müller, P. E., & Langer, N. 2012, *A&A*, **537**, A37
- Müller, P. E., & Vink, J. S. 2014, *A&A*, **564**, A57
- Najarro, F., Hanson, M. M., & Puls, J. 2011, *A&A*, **535**, A32
- Nesterov, V. V., Kuzmin, A. V., Ashimbaeva, N. T., et al. 1995, *A&AS*, **110**, 367
- Owocki, S. P., Castor, J. I., & Rybicki, G. B. 1988, *ApJ*, **335**, 914
- Owocki, S. P., Cranmer, S. R., & Gayley, K. G. 1996, *ApJL*, **472**, L115
- Parthasarathy, M., Drilling, J. S., Vijapurkar, J., & Takeda, Y. 2012, *PASJ*, **64**, 57
- Pauldrach, A. W. A., & Puls, J. 1990, *A&A*, **237**, 409
- Pecaut, M. J., & Mamajek, E. E. 2013, *ApJS*, **208**, 9
- Peri, C. S., Benaglia, P., & Isequilla, N. L. 2015, *A&A*, **578**, A45
- Perryman, M. A. C., Lindegren, L., Kovalevsky, J., et al. 1997, *A&A*, **323**, 49
- Petrov, B., Vink, J. S., & Gräfener, G. 2016, *MNRAS*, **458**, 1999
- Povich, M. S., Benjamin, R. A., Whitney, B. A., et al. 2008, *ApJ*, **689**, 242
- Prinja, R. K., & Massa, D. L. 2010, *A&A*, **521**, L55
- Puls, J., Kudritzki, R.-P., Herrero, A., et al. 1996, *A&A*, **305**, 171
- Puls, J., Sundqvist, J. O., & Markova, N. 2015, in *IAU Symp. 307, New Windows on Massive Stars*, ed. G. Maynet et al. (Cambridge: Cambridge Univ. Press), 25
- Puls, J., Urbaneja, M. A., Venero, R., et al. 2005, *A&A*, **435**, 669
- Puls, J., Vink, J. S., & Najarro, F. 2008, *A&ARv*, **16**, 209
- Randall, S. K., Bagnulo, S., Ziegerer, E., Geier, S., & Fontaine, G. 2015, *A&A*, **576**, A65
- Reed, B. C. 2003, *AJ*, **125**, 2531
- Reid, M. J., & Brunthaler, A. 2004, *ApJ*, **616**, 872
- Repolust, T., Puls, J., & Herrero, A. 2004, *A&A*, **415**, 349
- Robitaille, T. P., Meade, M. R., Babler, B. L., et al. 2008, *AJ*, **136**, 2413
- Sana, H., de Mink, S. E., de Koter, A., et al. 2012, *Sci*, **337**, 444
- Schönrich, R., Binney, J., & Dehnen, W. 2010, *MNRAS*, **403**, 1829
- Smith, N. 2014, *ARA&A*, **52**, 487
- Sota, A., Maíz Apellániz, J., Morrell, N. I., et al. 2014, *ApJS*, **211**, 10
- Sota, A., Maíz Apellániz, J., Walborn, N. R., et al. 2011, *ApJS*, **193**, 24
- Sperauskas, J., Bartašiūtė, S., Boyle, R. P., et al. 2016, *A&A*, **596**, A116
- Stephenson, C. B., & Sanduleak, N. 1971, *PW&SO*, **1**, 1
- Tarango-Yong, J. A., & Henney, W. J. 2018, *MNRAS*, **477**, 2431
- Tenorio-Tagle, G. 1979, *A&A*, **71**, 59
- Tjin A Djie, H. R. E., van den Ancker, M. E., Blondel, P. F. C., et al. 2001, *MNRAS*, **325**, 1441
- Tody, D. 1986, *Proc. SPIE*, **627**, 733
- Vijapurkar, J., & Drilling, J. S. 1993, *ApJS*, **89**, 293
- Vink, J. S. 2018, *A&A*, **619**, A54
- Vink, J. S., Brott, I., Gräfener, G., et al. 2010, *A&A*, **512**, L7
- Vink, J. S., de Koter, A., & Lamers, H. J. G. L. M. 1999, *A&A*, **350**, 181
- Vink, J. S., de Koter, A., & Lamers, H. J. G. L. M. 2000, *A&A*, **362**, 295
- Vink, J. S., de Koter, A., & Lamers, H. J. G. L. M. 2001, *A&A*, **369**, 574
- Wilkin, F. P. 1996, *ApJL*, **459**, L31
- Wilkin, F. P. 2000, *ApJ*, **532**, 400
- Wilson, J. C., Henderson, C. P., Herter, T. L., et al. 2004, *Proc. SPIE*, **5492**, 1295
- Xu, Y., Bian, S. B., Reid, M. J., et al. 2018, *A&A*, **616**, L15